

Article

Advanced Computational Framework to Analyze the Stability of Non-Newtonian Fluid Flow through a Wedge with Non-Linear Thermal Radiation and Chemical Reactions

Muhammad Imran Khan ¹, Ahmad Zeeshan ¹ , Rahmat Ellahi ^{1,2}  and Muhammad Mubashir Bhatti ^{3,*} 

¹ Department of Mathematics and Statistics, International Islamic University, Islamabad 44000, Pakistan; muhammad.phdma132@iiu.edu.pk (M.I.K.); ahmad.zeeshan@iiu.edu.pk (A.Z.); rellahi@alumni.ucr.edu (R.E.)

² Center for Modeling & Computer Simulation, Research Institute, King Fahd University of Petroleum & Minerals, Dhahran 31261, Saudi Arabia

³ College of Mathematics and Systems Science, Shandong University of Science and Technology, Qingdao 266590, China

* Correspondence: mmbhatti@sdust.edu.cn

Abstract: The main idea of this investigation is to introduce an integrated intelligence approach that investigates the chemically reacting flow of non-Newtonian fluid with a backpropagation neural network (LMS-BPNN). The AI-based LMS-BPNN approach is utilized to obtain the optimal solution of an MHD flow of Eyring–Powell over a porous shrinking wedge with a heat source and nonlinear thermal radiation (Rd). The partial differential equations (PDEs) that define flow problems are transformed into a system of ordinary differential equations (ODEs) through efficient similarity variables. The reference solution is obtained with the `bvp4c` function by changing parameters as displayed in Scenarios 1–7. The label data are divided into three portions, i.e., 80% for training, 10% for testing, and 10% for validation. The label data are used to obtain the approximate solution using the activation function in LMS-BPNN within the MATLAB built-in command ‘`nftool`’. The consistency and uniformity of LMS-BPNN are supported by fitness curves based on the MSE, correlation index (R), regression analysis, and function fit. The best validation performance of LMS-BPNN is obtained at 462, 369, 642, 542, 215, 209, and 286 epochs with MSE values of 8.67×10^{-10} , 1.64×10^{-9} , 1.03×10^{-9} , 302.935×10^{-10} , 8.56×10^{-10} , 1.08×10^{-9} , and 6.97×10^{-10} , respectively. It is noted that $f'(\eta)$, $\theta(\eta)$, and $\phi(\eta)$ satisfy the boundary conditions asymptotically for Scenarios 1–7 with LMS-BPNN. The dual solutions for flow performance outcomes (Cf_x , Nu_x , and Sh_x) are investigated with LMS-BPNN. It is concluded that when the magnetohydrodynamics increase ($M = 0.01, 0.05, 0.1$), then the solution bifurcates at different critical values, i.e., $\lambda_c = -1.06329, -1.097, -1.17694$. The stability analysis is conducted using an LMS-BPNN approximation, involving the computation of eigenvalues for the flow problem. The deduction drawn is that the upper (first) branch solution remains stable, while the lower branch solution causes a disturbance in the flow and leads to instability. It is observed that the boundary layer thickness for the lower branch (second) solution is greater than the first solution. A comparison of numerical results and predicted solutions with LMS-BPNN is provided and they are found to be in good agreement.

Keywords: artificial neural network (ANN); non-Newtonian fluid; wedge flow; stability analysis; non-linear thermal radiation

MSC: 68T07; 80A60; 76A05



Citation: Khan, M.I.; Zeeshan, A.; Ellahi, R.; Bhatti, M.M. Advanced Computational Framework to Analyze the Stability of Non-Newtonian Fluid Flow through a Wedge with Non-Linear Thermal Radiation and Chemical Reactions. *Mathematics* **2024**, *12*, 1420. <https://doi.org/10.3390/math12101420>

Academic Editor: Henar Herrero

Received: 25 March 2024

Revised: 25 April 2024

Accepted: 1 May 2024

Published: 7 May 2024



Copyright: © 2024 by the authors. Licensee MDPI, Basel, Switzerland. This article is an open access article distributed under the terms and conditions of the Creative Commons Attribution (CC BY) license (<https://creativecommons.org/licenses/by/4.0/>).

1. Introduction

Wedge flows are extremely important in many industries and engineering applications. Aerodynamic studies depend heavily on wedge flow, particularly to comprehend how flow behaves around airfoils and wings with acute leading edges. This information is essential

for creating stable and effective aircraft and other flying machines. There are many more applications of wedge flow such as blood flow around blood vessel bifurcations, tanks and reactors for chemical synthesis, and improving the blade design for wind turbines, etc. Boundary layer theory finds crucial applications in determining the skin friction drag experienced by bodies in motion through a fluid medium, including turbine blades, airplane wings, and ships. Falkner and Skan [1] were the first to present a model of wedge flow, based on fundamental principles of the Prandtl boundary layer theory. Subsequently, notable advancements have been achieved in this field with time. They used similarity transformations to convert the flow equations (PDEs) into nonlinear third-order ODEs. They investigated the effect of the pertained parameters of viscous fluids over stationary wedges. The aforementioned issue was expanded upon by Vajravelu and Nayfeh [2] and they scrutinized the impact of heat absorption on the hydromagnetic convection flow near a wedge. Non-Newtonian fluids have garnered significant attention in the field of fluid mechanics, finding applications in various industries, i.e., materials processing, aircraft, and energy systems. Non-Newtonian fluids are characterized by their shear-thinning or shear-thickening properties. Several fluid models have been developed over wedge flow to capture their viscosity dependence, including the Casson fluid, Maxwell fluid, Eyring–Powell fluid, Carreau fluid, and Williamson fluid models. Non-Newtonian fluids have gained prominence, particularly in different flow scenarios, such as the movement of hybrid nanofluid over shrinking surfaces. The Eyring–Powell model is based on a kinetic molecular model of liquids. It is rooted in the kinetic theory of liquids, providing a solid foundation rather than relying solely on empirical relationships. Secondly, it exhibits Newtonian behavior at both low and high shear rates [3]. Hussain et al. [4] discussed the numerical investigation of the chemical reaction of non-Newtonian fluid over a porous wedge. Gireesha et al. [5] looked closely at the Eyring–Powell nano liquid on a revolving and moving disc surface. Ali and Zaib [6] explored the stagnation point flow of the non-Newtonian nanofluid under convective conditions. Ahmed et al. [7] examined numerical investigation for gyrotactic microorganisms for a moving/static wedge. Numerous researchers have examined the transport phenomena of different non-Newtonian fluid models in various contexts [8–11].

The investigation of magnetohydrodynamic (MHD) boundary layers has captivated the interest of diverse scholars in recent decades due to its extensive relevance across industrial and technology domains. The presence of magnetic particles within a fluid has the potential to alter its magnetic characteristics. The presence of MHD in fluid increases the heat transfer coefficient. This heat transfer enhancement has various applications, i.e., cooling in electronics appliances, nuclear reactors, and many industrial processes. Fluid transportation systems can use MHD to reduce fluid friction in pipelines and channels, which results in energy savings. MHD can be used to manipulate electrically conductive fluids inside biological systems to create medical devices like drug delivery systems and diagnostic tools. MHD sensors can identify fluid characteristics like velocity, conductivity, and composition, providing real-time data for numerous industrial and scholarly applications. Yih [12] and Chamkha [13] delved into a numerical examination of the impact of MHD on flow scenarios involving viscous fluids over non-isothermal wedges. To explore further uses of MHD in the transport phenomena of fluid, see Refs. [14–17].

When we discuss the system's behavior, it is crucial to scrutinize the stability of a system. In fluid dynamics, stability is concerned with flow behavior. Fluid tends to become unstable for a definite range of physical parameters. Instability in a fluid flow over the shrinking surfaces arises due to vorticity inside the boundary layer and reveals the flow's non-uniqueness. Therefore, stability analysis is crucial in identifying flow behavior that is stable and physically meaningful. Science and engineering both rely heavily on stability to comprehend natural events. The researchers and scientists manipulate the flow control strategies and find the flow stable region. They investigate the range of certain physical parameters which affect flow behavior. The stability analysis aids in the optimization of the boundary layer and this technique is used to reduce the drag force. With this technique, we

can enhance the aerodynamics performance. The stability analysis of the shrinking surface included contributions from various academics. Awaludin et al. [18] examined the stability of MHD flow over a porous contracting/expanding wedge. Anuar et al. [19] investigated the stability analysis of the hybrid nanofluid over an exponentially shrinking sheet with a suction/injection effect on the stagnation point. They concluded that the non-unique nature of a solution exists for a definite range of physical parameters. Waini et al. [20] investigated the stability analysis of MHD boundary layer flow and heat transfer of hybrid nanofluid past a permeable shrinking wedge. They explored the effects of shrinking parameters and concentration of nanoparticles on the flow stability of a hybrid nanofluid. Mustafa et al. [21] scrutinized the stability of flow over a porous lessening sheet. They obtained a dual solution to the flow problem using the least squares method for some values of λ (velocity ratio parameter) and the magnetic parameter. They plotted Cf_x and Nu_x and demonstrated the range of dual solutions for certain physical parameters. Kasmani et al. [22] observed the examination of chemical reactions on the flow behavior of nanofluid over a porous wedge with heat generation/absorption during convective heat transfer. The stability analysis of surfaces undergoing reduction/extension has captured the interest of numerous researchers, like Pop [23], Zainal [24], Mishra [25], Hamid [26], Aberoumand [27], and Lund [28].

Computational fluid dynamics (CFD) and machine-learning algorithms are two artificial intelligence (AI) methods that can be used to explain and predict fluid flow patterns in complex geometries. Engineers can optimize designs to improve efficacy and performance by using AI-driven simulations to analyze fluid behavior. Moreover, AI can be used to create control techniques that modify fluid flows, improving qualities like lift, mixing, and other desired attributes. These methods are implemented to enhance the productivity of industrial processes, vehicles, and aircraft. Artificial neural networks (ANNs) have various applications in the simulation of boundary layer flow, including modeling the effect of boundary layer wind tunnel conditions, solving viscous and thermal boundary layer problems, and enabling the solution to thin boundary layers with singular perturbation problems. ANNs can be used with BPNN which is a well-known optimization technique to enhance the fluid flow system performance and design. ANNs can assist in identifying the best configurations to accomplish desired goals like decreasing drag or improving efficiency. ANNs have been used to predict the mean velocity, turbulence intensity, and model length scale factor in boundary layer wind tunnel profiles. Additionally, they have been employed in predicting turbulent channel and separated boundary-layer flows, as well as in developing prediction models for compressible turbulent boundary-layer flow over a smooth flat surface. These applications demonstrate the effectiveness of ANNs in simulating and understanding complex boundary layer phenomena. Zeeshan et al. [29] investigated the impact of thermal radiation and MHD on the boundary layer flow of Casson ternary hybrid nanofluid with artificial neural network simulation. Das and Reddy [30] examined the MHD boundary layer flow for the first time with ANN estimation over a porous extending cylinder. Shoaib et al. [31] examined the impact of thermal radiation (R) on MHD Casson fluid over a porous surface. They determined that the temperature of the surface decreases when thermal radiation (Rd) rises. Awais et al. [32] developed an ANN algorithm to investigate the transport phenomena through a porous surface. Reddy et al. [33] developed a machine-learning scheme to analyze the effects of activation energy on an MHD nanofluid flow over an extending sheet. Mishra et al. [34] examined the heat transfer of ternary hybrid nanofluid with three different geometry with ANNs. There is a variety of research conducted on the boundary layer flow with ANNs over different geometries [29,35–38].

To the author's knowledge, there is a lack of prior research on the use of an ANN model to analyze the flow stability of MHD boundary layer flows over a porous contracting wedge. According to a literature review, ANN models have proven to be highly effective in obtaining approximate solutions to nonlinear problems. The current work therefore focuses

on ANN approximation to analyze the flow stability over a porous contracting wedge. The novelty and uniqueness of the present study are highlighted in the following lines:

- The chemically reacting flow of non-Newtonian fluid has been studied, taking into account the properties of a heat source on a porous shrinking wedge.
- The impacts of the temperature ratio parameter on the heat transfer coefficient are also considered to enhance the novelty of the present work.
- The current study examines the impact of many pertinent factors and results are displayed graphically.
- To enhance the novelty and uniqueness of the latest research, we used a supervised machine-learning (ANN with BPNN) approach to analyze the flow stability.

2. Materials and Methods

Consider the scenario of a chemically reacting flow of a two-dimensional model of non-Newtonian fluid over a porous shrinking wedge with nonlinear thermal radiation (Rd) and a heat source. The depiction of the flow geometry is illustrated in Figure 1, with Cartesian coordinates denoted as x and y . The shrinking wall surface has a velocity $u_w(x) = U_w x^m$ and free stream velocity, $u_e(x) = U_\infty x^m$. Here, u and v are horizontal and vertical components of velocity, respectively. We have $\beta = \Omega/\pi$ with Ω as the total angle of a wedge [39] and m as the wedge angle parameter. It is noticed that $0 \leq m \leq 1$. T_w and C_w are constant temperature and concentration at the wall of a wedge where T_∞ is the ambient temperature and C_∞ is the concentration of fluid far away from the wedge. Additionally, the magnetic field $B(x) = B_0 x^{\frac{m-1}{2}}$ is introduced at an inclined angle Ψ with B_0 the strength of the magnetic field. If $\Psi = \pi/2$, then the magnetic field is applied perpendicular. The governing equations of the flow under consideration are as follows [39–44]:

$$\frac{\partial u}{\partial x} + \frac{\partial v}{\partial y} = 0, \tag{1}$$

$$u \frac{\partial u}{\partial x} + v \frac{\partial u}{\partial y} = u_e \frac{du_e}{dx} + \left(v + \frac{1}{\rho \wedge d} \right) \frac{\partial^2 u}{\partial y^2} - \frac{1}{2\rho d^3 \wedge} \left(\frac{\partial u}{\partial y} \right)^2 \frac{\partial^2 u}{\partial y^2} + [\beta_0 g(T - T_\infty) + (C - C_\infty)\beta_0 g] \sin\left(\frac{\Omega}{2}\right) - \frac{\sigma B^2(x)}{\rho} \sin^2(\Psi)(u - u_e) \tag{2}$$

$$u \frac{\partial T}{\partial x} + v \frac{\partial T}{\partial y} = \frac{k}{\rho C_p} \frac{\partial^2 T}{\partial y^2} - \frac{1}{\rho C_p} \left(\frac{\partial q_r}{\partial y} \right) + \frac{Q(x)}{\rho C_p} (T - T_\infty), \tag{3}$$

$$u \frac{\partial C}{\partial x} + v \frac{\partial C}{\partial y} = D_B \frac{\partial^2 C}{\partial y^2} - k_1 (C - C_\infty). \tag{4}$$

where β_0 is the thermal expansion and g is an acceleration due to gravity. ν is the fluid viscosity and d represents a rheological constant. The thermal radiation with heat generation/absorption effects is introduced. With the use of the Rosseland approximation [40], we define thermal radiation as $q_r = -\frac{4\sigma^*}{3k^*} \frac{\partial T^4}{\partial y} = -16 \frac{\sigma^*}{k^*} \frac{\partial T}{\partial y}$. We suppose the nonlinear radiation effect; therefore the temperature should be $T = T_\infty(1 + (\theta_w - 1)\theta)$, where $\theta_w = \frac{T_w}{T_\infty}$ [40–44]. The chemical reaction equation has been introduced to enhance the novelty of the present work, whereas D_B is molecular diffusivity of the species concentration and k_1 is a chemical reaction parameter [39]. The boundary conditions of the flow problem are as follows:

$$u = u_w, v = v_w, T = T_w + bx^2, C = C_w, \text{ at } y = 0, u \rightarrow u_e(x), T \rightarrow T_\infty, C \rightarrow C_\infty, \text{ at } y \rightarrow \infty \tag{5}$$

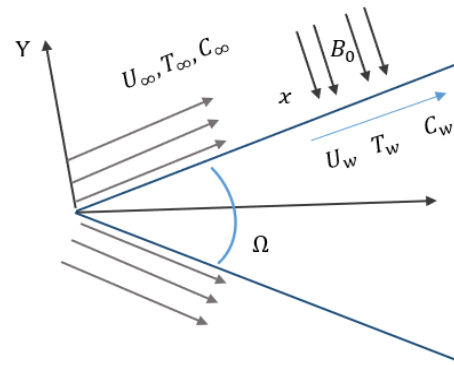


Figure 1. Flow geometry.

The partial differential equations (PDEs) (1)–(4) of the considered flow problem over a porous shrinking wedge are transformed into ordinary differential equations (ODEs) with similarity variables defined as below [39,40]:

$$\psi = \sqrt{\frac{2\nu x u_e(x)}{1+m}} f(\eta), \quad \eta = \sqrt{\frac{(1+m)u_e(x)}{2\nu x}} y, \quad \theta(\eta) = \frac{T - T_\infty}{T_w - T_\infty}, \quad \phi(\eta) = \frac{C - C_\infty}{C_w - C_\infty}. \quad (6)$$

ψ , is the stream function, θ is a dimensionless temperature and ϕ is the dimensionless concentration. The velocity components in terms of stream function ψ are defined as $u = \frac{\partial \psi}{\partial y}$ and $v = -\frac{\partial \psi}{\partial x}$. However, the velocity components using the similarity transformations Equation (6) becomes the following [18,39,40]:

$$u = u_e f'(\eta), \quad v = -\sqrt{\frac{(1+m)\nu u_e}{2x}} \left[f(\eta) + \frac{m-1}{m+1} \eta f'(\eta) \right] \quad (7)$$

The continuity Equation (1) is satisfied identically. Moreover, Equations (2)–(4) of flow problem is transformed into a dimensionless ordinary differential equation as follows:

$$(1+W)f''' - \frac{\delta W}{2} f''' (f'')^2 + f f'' - \beta(1-f'^2) + M \sin^2 \Psi (1-f') + (Gr\theta + Gc\phi) \sin\left(\frac{\alpha}{2}\right) = 0 \quad (8)$$

$$\frac{1}{Pr} \left(1 + \frac{4}{3} Rd \left(((\theta_w - 1)\theta + 1)^3 \right) \right) \theta'' + 4Rd \left(((\theta_w - 1)\theta + 1)^2 (\theta_w - 1) \theta'^2 \right) + f\theta' - 2\beta f'\theta + Q(2-\beta)\theta = 0 \quad (9)$$

$$\phi'' - Sc \left(K_c(2-\beta)\phi + 2\beta(f'\phi - f\phi') \right) = 0 \quad (10)$$

The dimensionless boundary conditions for Equations (8)–(10) are transformed:

$$f(0) = S, \quad f'(0) = \lambda, \quad \theta(0) = 1, \quad \phi(0) = 1, \quad f'(\eta) \rightarrow 1, \quad \theta(\eta) = 0, \quad \phi(\eta) = 0, \quad \text{as } \eta \rightarrow \infty. \quad (11)$$

The physical parameters of interest arise in Equations (8)–(10) and the boundary conditions in Equation (11) are defined as follows: $W = \frac{1}{\mu \wedge d}$, where $\delta = \frac{u_e^3}{\nu d^2} \frac{m+1}{2}$ represents the Eyring–Powell fluid constant [39,40]. $M = \frac{2\sigma B_0^2}{\rho U_\infty (m+1)}$ is the magnetic field constant [41], $\lambda = \frac{U_w}{U_\infty}$ is the shrinking and stretching parameter, $Rd = \frac{4\sigma^* T_\infty^3}{3k^*}$ is the thermal radiation parameter, $Sc = \frac{\nu}{D_m}$ is the Schmidt number, and $K_c = \frac{k_1}{\nu}$ is the chemical reaction parameter [39,45]. If $K_c > 0$, this shows a constructive/generative reaction, and $K_c < 0$ is a destructive chemical reaction. We consider the generative reaction. $\theta_w = \frac{T_w}{T_\infty}$ is the temperature difference parameter, $Gr = \frac{g\beta_o(T_w - T_\infty)L^3}{(m+1)\nu^2}$ is the Grashof number, $Gc = \frac{g\beta_o(C_w - C_\infty)L^3}{(m+1)\nu^2}$ is the mass Grashof number [33,39], $S = \nu_w \sqrt{\frac{2x}{(m+1)u_e}}$ is the suction/injection parameter [39],

and $Re = \frac{u_e L}{\nu}$ is the Reynolds number. The physical output responses of interest are Cf_x , Nu_x , and Sh_x [39,40].

$$Cf_x = \frac{\tau_w}{\rho u_e^2(x)}, Nu_x = \frac{xq_w}{k(T_w - T_\infty)}, Sh_x = \frac{xq_m}{D_b(C_w - C_\infty)} \tag{12}$$

where $\tau_w = \mu \left(\frac{\partial u}{\partial y} \right)_{y=0}$, $q_w = -k \left(\frac{\partial T}{\partial y} \right)_{y=0} + q_r$, and $q_m = D_b \left(\frac{\partial C}{\partial y} \right)_{y=0}$ [39–41]. The stress tensor for Eyring–Powell fluid [39] over the wedge is defined as follows:

$$\tau_w = \left(\mu + \frac{1}{\wedge d} \right) \frac{\partial u_i}{\partial x_j} - \frac{1}{6 \wedge d^3} \left(\frac{\partial u_i}{\partial x_j} \right)^3 \tag{13}$$

By using Equations (6), and (13) in Equation (12), we obtained the output response of flow quantities as follows [39,40]:

$$CfRe_x^{\frac{1}{2}} = (1 + W)f''(0) - \frac{\delta W}{3}(f''(0))^3, NuRe_x^{-\frac{1}{2}} \sqrt{\frac{2}{m+1}} = - \left(1 + \frac{4}{3} Rd(1 + (\theta_w - 1)\theta(0))^3 \right) \theta'(0), \tag{14}$$

$$ShRe_x^{-\frac{1}{2}} \sqrt{\frac{2}{m+1}} = -\phi'(0).$$

Stability Analysis

The stability analysis of flows is essential for understanding the behavior of fluids in various engineering and natural systems. To examine flow stability, there are several instruments, including the Reynolds number, the Euler equations and Lagrangian perturbation theory, computational techniques, and linear stability analysis which entails linearizing the Navier–Stokes equations concerning a base flow and solving linear equations to investigate the flow properties. Examining the flow field’s stability properties with time is usually the first step in analyzing the temporal stability analysis of fluid dynamics in wedge flow. Understanding how disruptions or variations in the flow change over time and whether the flow is stable or unstable depends on this analysis. The authors perform a linear stability study to examine the temporal evolution of minor perturbations in the flow. Usually, this involves resolving eigenvalue issues related to the linearized equations. The eigenvalues reveal if the perturbations increase, decrease, or stay the same. Therefore, a temporal stability analysis is executed, to investigate the impact of the pertained parameters on the flow performance quantities, i.e., skin friction coefficient, Nusselt number, and Sherwood number. The unsteady case is discussed to perform stability analysis [39–43]:

$$\frac{\partial u}{\partial t} + u \frac{\partial u}{\partial x} + v \frac{\partial u}{\partial y} = U_e \frac{dU_e}{dx} + \left(\nu + \frac{1}{\rho \wedge d} \right) \frac{\partial^2 u}{\partial y^2} - \frac{1}{2\rho d^3 \wedge} \left(\frac{\partial u}{\partial y} \right)^2 \frac{\partial^2 u}{\partial y^2} + [\beta_0 g(T - T_\infty) + (C - C_\infty)\beta_0 g] \sin\left(\frac{\Omega}{2}\right) - \frac{\sigma B^2(x)}{\rho} \sin^2(\Psi)(u - U_e) \tag{15}$$

$$\frac{\partial T}{\partial t} + u \frac{\partial T}{\partial x} + v \frac{\partial T}{\partial y} = \frac{k}{\rho C_p} \frac{\partial^2 T}{\partial y^2} + \frac{16\sigma}{3K^* \rho C_p} \frac{\partial^2 T^4}{\partial y^2} + \frac{Q(x)}{\rho C_p} (T - T_\infty) \tag{16}$$

$$\frac{\partial C}{\partial t} + u \frac{\partial C}{\partial x} + v \frac{\partial C}{\partial y} = D_B \frac{\partial^2 C}{\partial y^2} - k_1(C - C_\infty) \tag{17}$$

where t denotes time. Therefore, the new similarity transformation becomes the following:

$$\psi = \sqrt{\frac{2\nu x u_e}{1+m}} f(\eta, \tau), \eta = \sqrt{\frac{(1+m)u_e}{2\nu x}} y, \theta(\eta, \tau) = \frac{T - T_\infty}{T_w - T_\infty}, \phi(\eta, \tau) = \frac{C - C_\infty}{C - C_\infty}, \tau = \frac{1+m}{2} \left(\frac{u_e}{x} \right) t. \tag{18}$$

τ is a dimensionless time; the new similarity variables in Equation (18) are used to change the flow Equations (15)–(17) to the following differential equations:

$$(1+W) \frac{\partial^3 f}{\partial \eta^3} - \frac{\delta W}{2} \frac{\partial^3 f}{\partial \eta^3} \left(\frac{\partial^2 f}{\partial \eta^2} \right)^2 + f \frac{\partial^2 f}{\partial \eta^2} - \beta \left(1 - \left(\frac{\partial f}{\partial \eta} \right)^2 \right) + M \sin^2 \Psi \left(1 - \frac{\partial f}{\partial \eta} \right) + (Gr\theta + Gc\phi) \sin\left(\frac{\alpha}{2}\right) - \frac{\partial^2 f}{\partial \eta \partial \tau} = 0 \tag{19}$$

$$\frac{1}{Pr} \left(1 + \frac{4}{3} Rd \left(((\theta_w - 1)\theta + 1)^3 \right) \right) \frac{\partial^2 \theta}{\partial \eta^2} + 4Rd \left(((\theta_w - 1)\theta + 1)^2 (\theta_w - 1) \left(\frac{\partial \theta}{\partial \eta} \right)^2 \right) + f \frac{\partial \theta}{\partial \eta} - 2\beta \frac{\partial f}{\partial \eta} \theta + Q(2 - \beta)\theta - \frac{\partial \theta}{\partial \tau} = 0 \tag{20}$$

$$\frac{\partial^2 \phi}{\partial \eta^2} - Sc(K_c(2 - \beta)\phi + 2\beta \left(\frac{\partial f}{\partial \eta} \phi - f \frac{\partial \phi}{\partial \eta} \right)) - \frac{\partial \phi}{\partial \tau} = 0 \tag{21}$$

Now, we define the corresponding boundary conditions:

$$f(0, \tau) = S, \quad \frac{\partial f}{\partial \eta}(0, \tau) = \lambda, \quad \theta(0, \tau) = 1, \quad \phi(0, \tau) = 1, \quad \text{at } \eta = 0, \tag{22}$$

$$\frac{\partial f}{\partial \eta}(\eta, \tau) \rightarrow 1, \quad \theta(\eta, \tau) = 0, \quad \phi(\eta, \tau) = 0, \quad \eta \rightarrow \infty.$$

To test the stability of flow behavior, use the regular perturbation expansion to evaluate the eigenvalue (see References [46,47]). Many more researchers use the same concept to study the stability of the boundary layer flow over the shrinking surface: [48–51]. Consider, $f(\eta) = f_0(\eta)$, $\theta(\eta) = \theta_0(\eta)$, and $\phi(\eta) = \phi_0(\eta)$, see Merrill et al. [52]:

$$\begin{aligned} f(\eta, \tau) &= f_0(\eta) + \exp(-\gamma\tau)F(\eta, \tau), \\ \theta(\eta, \tau) &= \theta_0(\eta) + \exp(-\gamma\tau)G(\eta, \tau), \\ \phi(\eta, \tau) &= \phi_0(\eta) + \exp(-\gamma\tau)H(\eta, \tau). \end{aligned} \tag{23}$$

Here, γ is defined as the eigenvalue, $F(\eta, \tau)$, $G(\eta, \tau)$, and $H(\eta, \tau)$ are small as compared to $f_0(\eta)$, $\theta_0(\eta)$, and $\phi_0(\eta)$; for details, see References [46–52]. From Equations (19)–(21), we have an infinite set of eigenvalues $\gamma_1 < \gamma_2 < \gamma_3 < \dots$. These eigenvalues define the flow behavior. Substituting Equation (23) into Equations (19)–(21), we then obtain the following linear steady-state eigenvalues problems and as we discuss the steady state the derivative with τ vanishes [46–52]:

$$(1 + W)F''' - \frac{\delta W}{2} \left(f_0'^2 F''' + 2f_0'' f_0''' F'' \right) + f_0'' F + f_0 F'' - 2\beta f_0' F' - M \sin^2 \Psi F' + (GrG + GcH) \sin\left(\frac{\alpha}{2}\right) - \gamma F' = 0, \tag{24}$$

$$\begin{aligned} \frac{1}{Pr} G'' + \frac{1}{Pr} \left(\frac{4}{3} R(\theta_w - 1) \right) \{ (\theta_w - 1)^2 (3\theta_0^2 \theta_0'' G + \theta_0^3 G'') + 3(\theta_w - 1)(2\theta_0 \theta_0'' G + \theta_0^2 G'') + 3(\theta_0'' G + \theta_0 G'') \} + \\ (\theta_w - 1)^2 \{ (\theta_w - 1)(2\theta_0 \theta_0'^2 G + 2\theta_0^2 \theta_0' G') \} + \{ 4\theta_0' \theta_0 G' + 2\theta_0^2 G' \} + 2(\theta_w - 1)\theta_0' G' + f_0 G' + \theta_0' F + \\ 2\beta \{ f_0' G + \theta_0 F' \} + Q(2 - \beta)G - \gamma G = 0, \end{aligned} \tag{25}$$

$$H'' - Sc(K_c(2 - \beta))H + 2\beta \{ (f_0' H + \phi_0 F') - (f_0 H' + \phi_0' F) \} - \gamma H = 0. \tag{26}$$

The corresponding boundary conditions are as follows [18,19]:

$$\begin{aligned} F(0) = 0, \quad F'(0) = 0, \quad G(0) = 0, \quad H(0) = 0, \quad \text{at } \eta = 0, \\ F'(\eta) \rightarrow 0, \quad G(\eta) = 0, \quad H(\eta) = 0, \quad \eta \rightarrow \infty. \end{aligned} \tag{27}$$

3. Research Methodology

The authors focused on scrutinizing non-uniqueness and stability analysis of the flow response outcomes (Cf_x , Nu_x , and Sh_x) of an MHD boundary layer flow non-Newtonian fluid over a porous shrinking wedge with nonlinear thermal radiation analysis. To test the stability of flow, it is important to evaluate the eigenvalues of the differential equation of the proposed model. For this purpose, an unsteady case of the problem is defined and regular perturbation expansion to obtain the eigenvalue. The writers divide the research methodology into two phases. Firstly, the numerical data sheet of these flow response outcomes can be obtained by solving Equations (8) and (10) and boundary conditions (11) with bvp4c. Bvp4c is a MATLAB integrated package founded on the 3-stage Lobatto IIIa formula and finite-difference scheme. We use the proper initial approximations to attain a numerical solution. Secondly, an artificial neural network (ANN) is applied.

Artificial Neural Network

A broadly renowned domain within the realm of artificial intelligence (AI) investigation is the study of artificial neural networks (ANNs), which use a computational structure motivated by the organizational structure of the human brain. Robert Hecht-Nielsen [53], known for developing one of the pioneering neurocomputers, provides a clear and uncomplicated definition of artificial neural networks (ANNs). Artificial neural networking (ANN) unquestionably stands out as the most widely recognized technique in supervised learning [53–58]. The Levenberg–Marquardt scheme (LMS) is widely used for nonlinear optimizations problems. In the combination of BPNN, it helps in training the neural network more efficiently. The convergence rate of LMS-BPNN is faster to optimize the flow behavior in complex and high-dimensional data for the training of ANNs. The bvp4c along with LMS-BPNN is a powerful scheme to handle complex mathematical problems more efficiently and accurately.

They are basic nonlinear function approximations. ANNs derive their robustness and flexibility from their modular structure, which uses the neuron as the fundamental building unit, mimicking the neurons present in the human brain. An input is given to each neuron, which then processes it through an activation function to produce an output. Combining multiple neurons can result in the creation of various structures that convey information about the issue and the type of data. In neural network (NN) topologies, input layers receive the data, while output layers provide predictions. Nonlinear optimization techniques, i.e., backpropagation, are used to determine the network weights. This approach is used to enhance the uniformity and accuracy of the model's predictions. The neurons in artificial neural networks (ANNs) are arranged in layers. In a neural network, each layer's neurons receive input from the previous layer and transmit their output to the next layer. The performance of the suggested Eyring–Powell fluid model is investigated by LMS-BPNN. This analysis involves the fitness function, MSE, regression, and error histogram with the applications of the 'nftool command'. For implementing the proposed LMS-BPNN approach, the results concerning $f'(\eta)$, $\theta(\eta)$, and $\phi(\eta)$ profiles for inputs ranging from 0 to 3 exhibit considerable dispersion. The dataset is then partitioned into training (80%), validation (10%), and testing (10%) subsets (Appendix A). Figure 2 illustrates a schematic representation of a backpropagation neural network (BPNN) featuring n input nodes, r output nodes, and a solitary hidden layer comprising m nodes, whereas Figure 2b shows the multilayer ANN with $m = 10$. It means that we have 10 neurons in the hidden layers. Every connection linking the nodes possesses an assigned weight. The input nodes are characterized by a transfer function of unity, while the hidden and output nodes employ sigmoidal $S(\cdot)$ and activation functions, respectively (for detailed analysis of these functions, see Ref. [30]). The net input as shown in Figure 2a, is provided by the equation below:

$$y_j(x) = \sum_{i=1}^n w_{1ji}X_i + b_{1j}, \quad (28)$$

We define w_{1ji} as a weight, while b_{1j} is the bias at the j^{th} node. The output for the j^{th} node of the hidden layer is defined as follows:

$$Z_j(x) = \frac{1}{1 + \exp(-y_j(x))} \quad (29)$$

As in Figure 2a, $O_k(x)$ represents the output values of the k^{th} node defined as follows:

$$O_k(x) = \sum_{j=1}^m w_{2kj}Z_j + b_{2k} \quad (30)$$

where w_{2kj} is a weight function. An artificial neural network (ANN) produces its output by receiving inputs and calculating results depending on the activation of various nodes and their linked weights. An activation function receives a weighted input from each node in the network and produces an output that is then sent to the node after it.

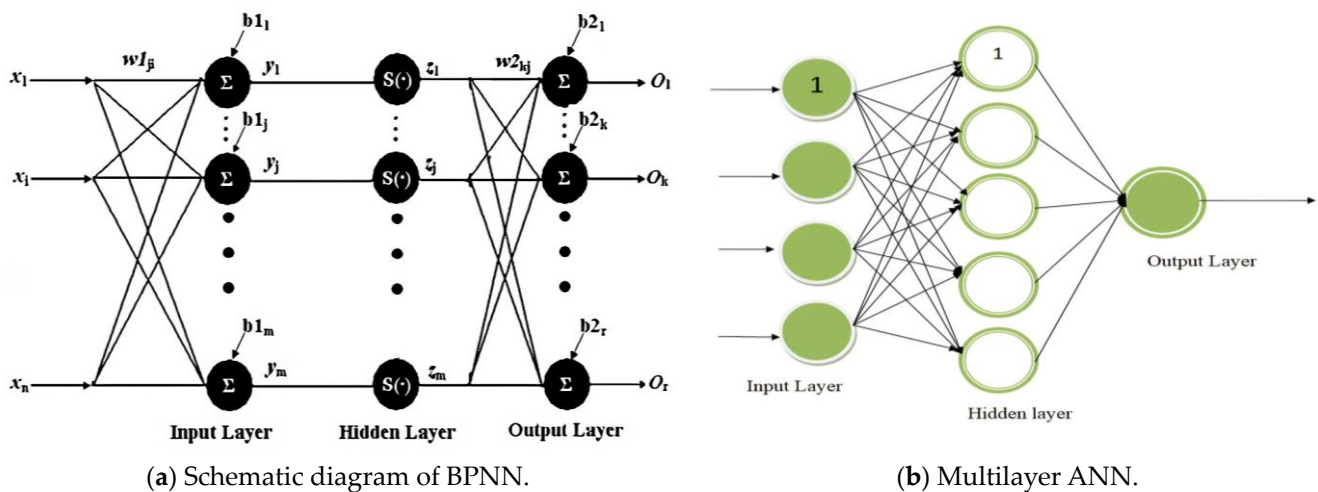
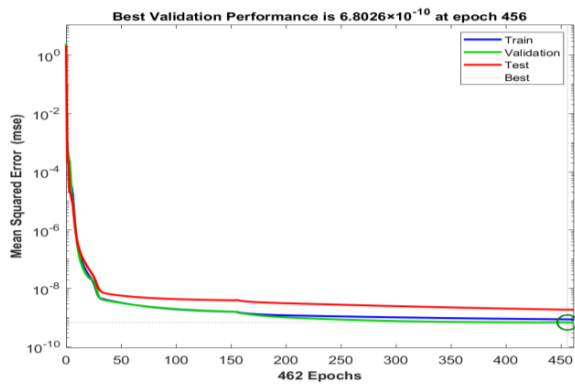


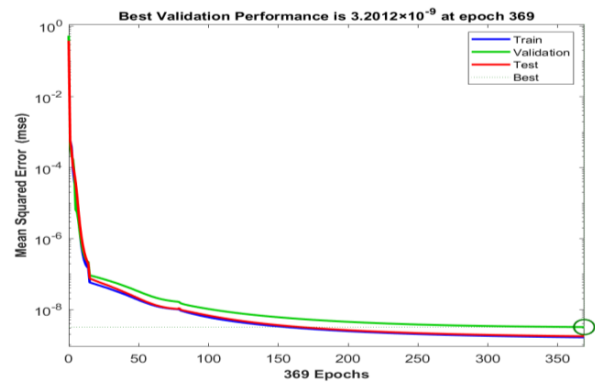
Figure 2. Structure of artificial neural networks.

4. Results and Discussion

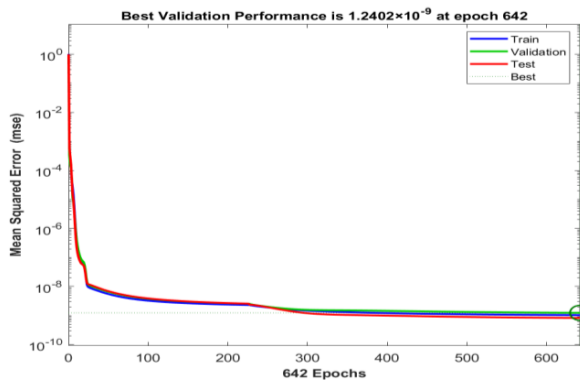
The AI-based LMS-BPNN framework has been developed to analyze the results of pertained parameters of interest (angle of inclination, M, S, λ, Q, R, Sc) for Eyring–Powell fluid flow over a porous shrinking wedge with nonlinear thermal radiation. By employing the LMS-BPNN framework, researchers can gain a deeper understanding of the complex interactions between fluid dynamics, heat transfer, and chemical reactions in the context of Eyring–Powell fluid flow over porous shrinking wedges with nonlinear thermal radiation. There are seven different scenarios which consist of three different cases of pertained parameters of interest as shown in Table 1. To validate the scenarios’ data, the correlation index (R), MSE, error histogram, regression analysis, and function fit are defined. The mean squared error (MSE) is a measure of error in statistical models that assesses the average squared difference between numerical and predicted values. The MSE is used to evaluate the quality of a model, with a smaller MSE indicating a better fit of the model to the data. Figures 3 and 4 demonstrate the evaluation of performance and the examination of errors using histograms for the different scenarios (Scenarios 1–7) as shown in Table 1. In Figure 3a–g, it is noticed that the MSE is approximately 10^{-8} for various scenarios as presented in Table 1. The graphical depiction of the distribution of errors between the observed and predicted approximate values in a model is called an error histogram. It aids in comprehending the model’s performance and spotting possible problems like overfitting or underfitting. Figure 5 depicts regression analysis for different scenarios with LMS-BPNN. It is important to remember that the fitness function must be properly developed to represent the objectives of the neural network training. The efficiency of the training process can also be affected by the optimization algorithm selection (i.e., LMS-BPNN) and its settings. Figure 6 represents the function fit for Scenarios 1–7 with Case 1. It is found that the function is best fitted with an approximate error analysis of 10^{-4} . Table 2 displays the convergence of labeled data for the proposed algorithm of LMS-BPNN for the first solution of the Eyring–Powell fluid for Scenarios 1–7 in terms of error analysis for different portions of divided data, iterations, and Mu . The best curve for the first solution of the seven scenarios is obtained at 462, 369, 642, 542, 215, 209, and 286 epochs, while the performance against these epochs/iterations is 8.67×10^{-10} , 1.64×10^{-9} , 1.03×10^{-9} , 9.35×10^{-10} , 8.56×10^{-10} , 1.08×10^{-9} , and 6.97×10^{-10} , respectively.



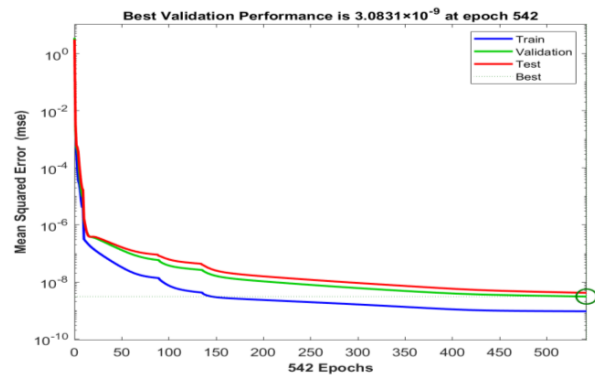
(a) Scenario 1 Case 1.



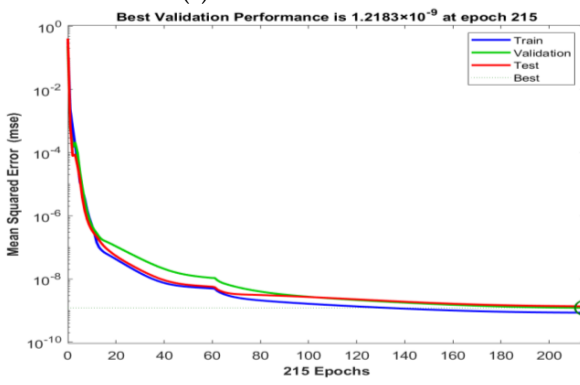
(b) Scenario 2 Case 1.



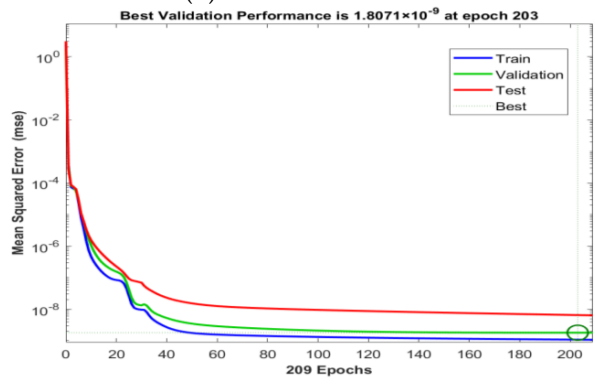
(c) Scenario 3 Case 1.



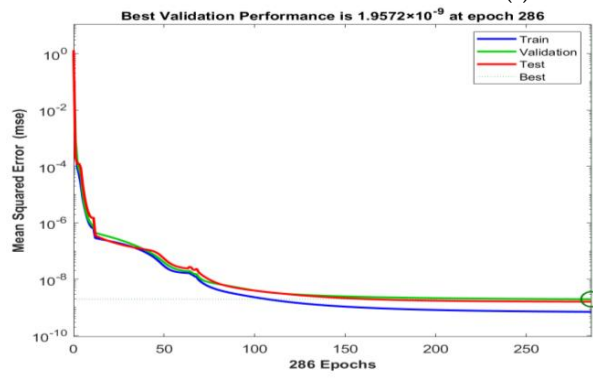
(d) Scenario 4 Case 1.



(e) Scenario 5 Case 1.

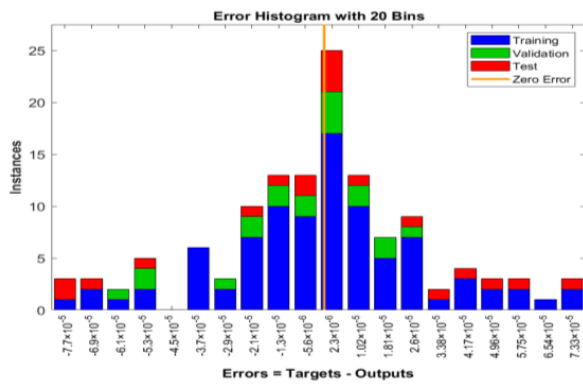


(f) Scenario 6 Case 1.

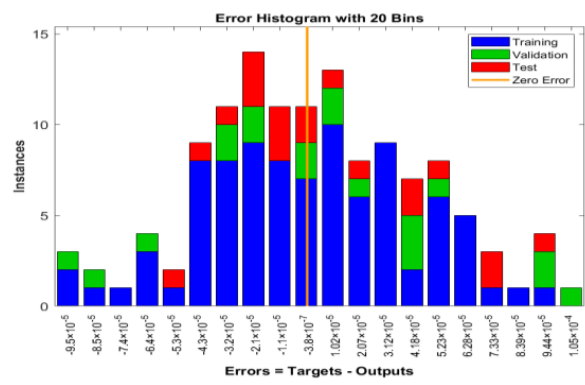


(g) Scenario 7 Case 1.

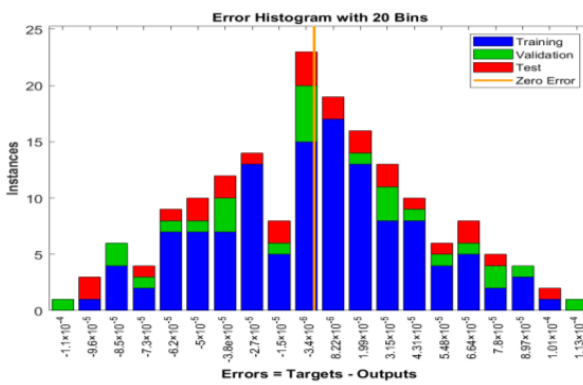
Figure 3. Mean squared error for the first solution of Scenarios 1–7 for Case 1 with intended LMS–BPNN.



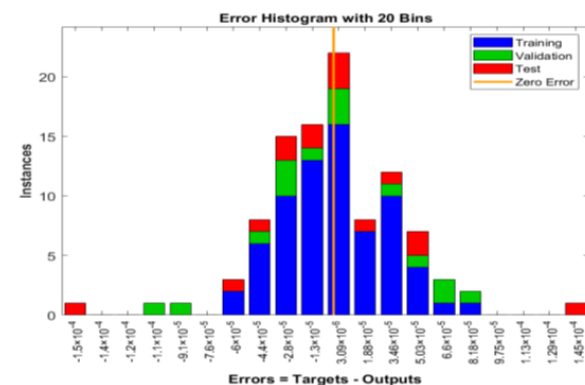
(a) Scenario 1 Case 1.



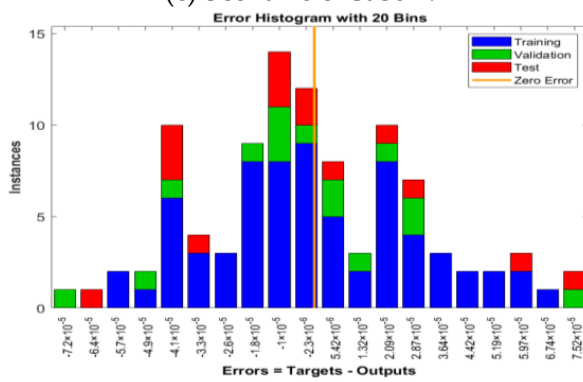
(b) Scenario 2 Case 1.



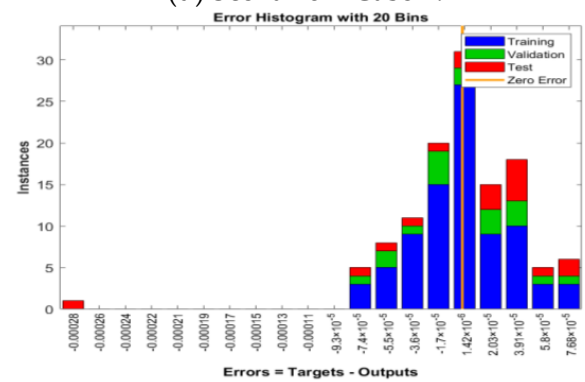
(c) Scenario 3 Case 1.



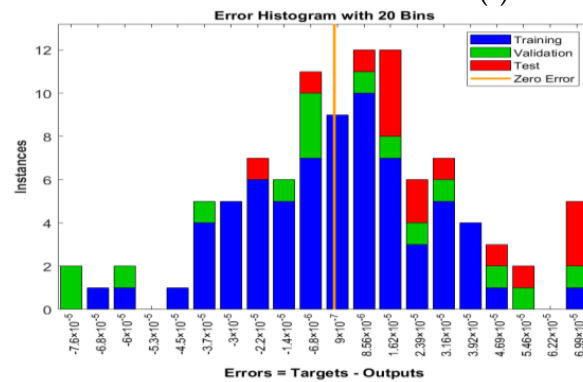
(d) Scenario 4 Case 1.



(e) Scenario 5 Case 1.



(f) Scenario 6 Case 1.

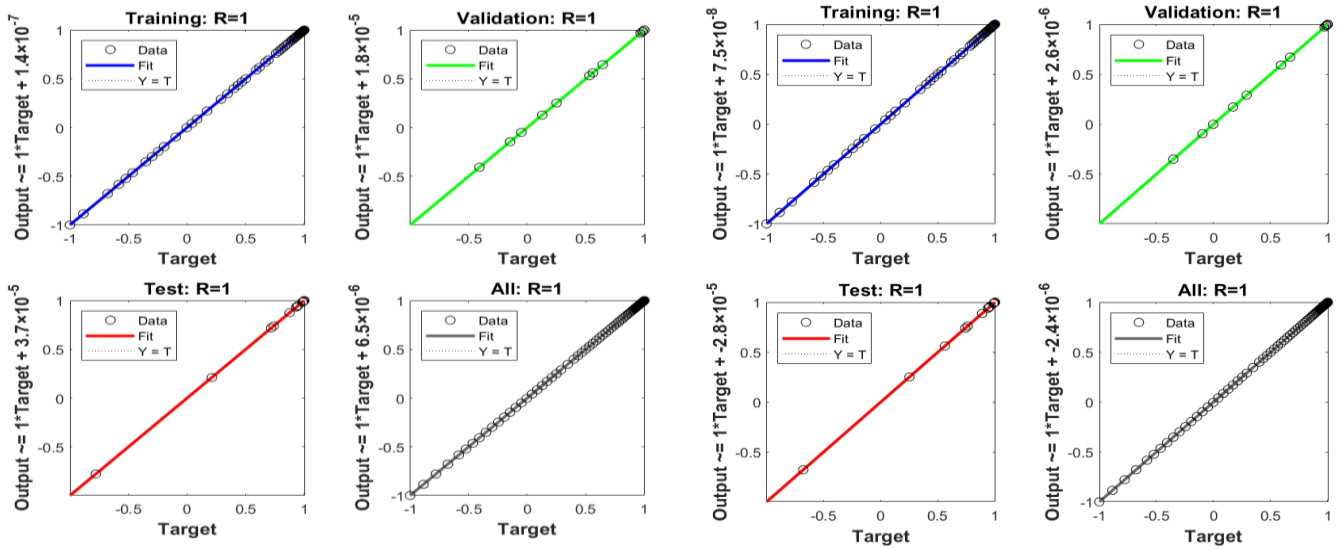


(g) Scenario 7 Case 1.

Figure 4. Error histogram for the first solution of Scenarios 1–7 for Case 1 with intended LMS–BPNN.

Table 1. Depiction for scenarios of Eyring–Powell fluid.

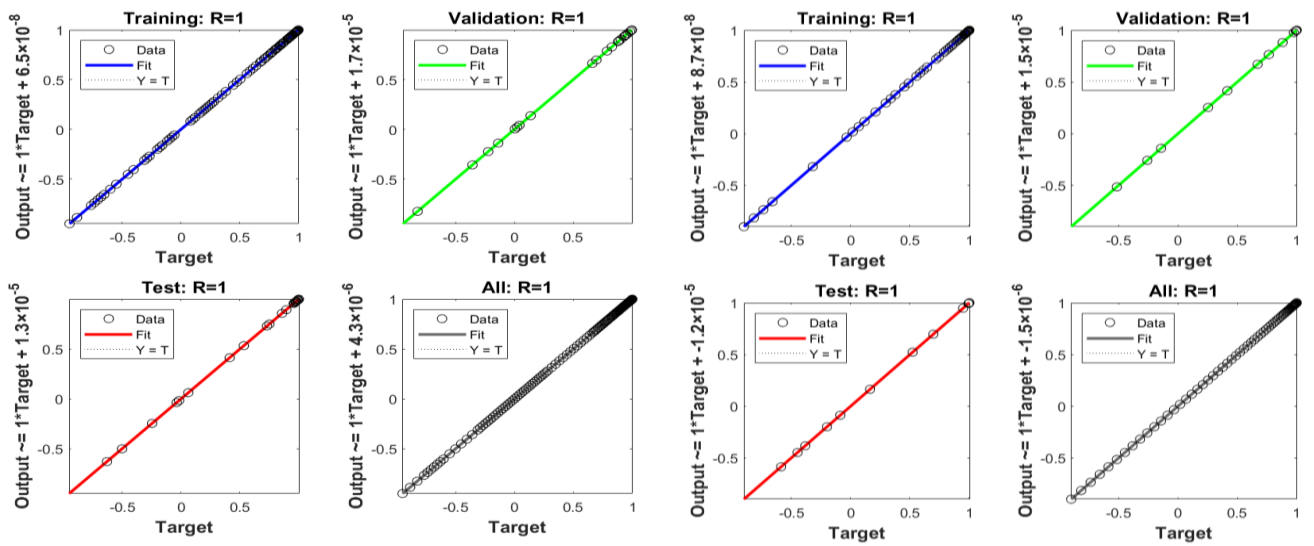
Scenario	Case	Input Parameters						
		Angle of Inclination	M	S	λ	Q	Rd	Sc
1	1	$\pi/6$						
	2	$\pi/3$						
	3	$\pi/2$						
2	1		0.01					
	2		0.05					
	3		0.1					
3	1			0.8				
	2			0.9				
	3			1				
4	1				-0.9			
	2				-1.03			
	3				-1.06			
5	1					0.01		
	2					0.05		
	3					0.1		
6	1						0.1	
	2						0.5	
	3						0.9	
7	1							0.5
	2							1
	3							1.5



(a) Scenario 1 Case 1.

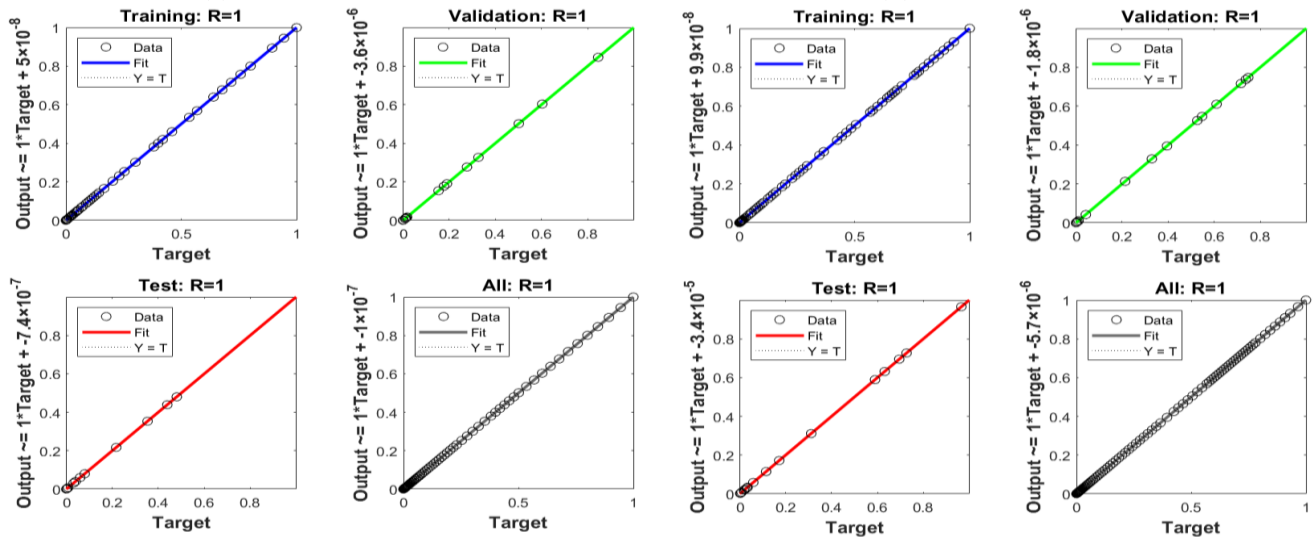
(b) Scenario 2 Case 1.

Figure 5. Cont.



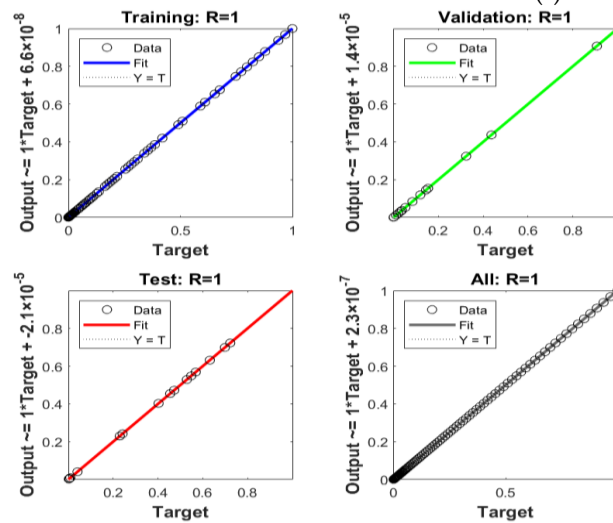
(c) Scenario 3 Case 1.

(d) Scenario 4 Case 1.



(e) Scenario 5 Case 1.

(f) Scenario 6 Case 1.



(g) Scenario 7 Case 1.

Figure 5. Regression analysis for the first solution of Scenarios 1–7 for Case 1 with intended LMS–BPNN.

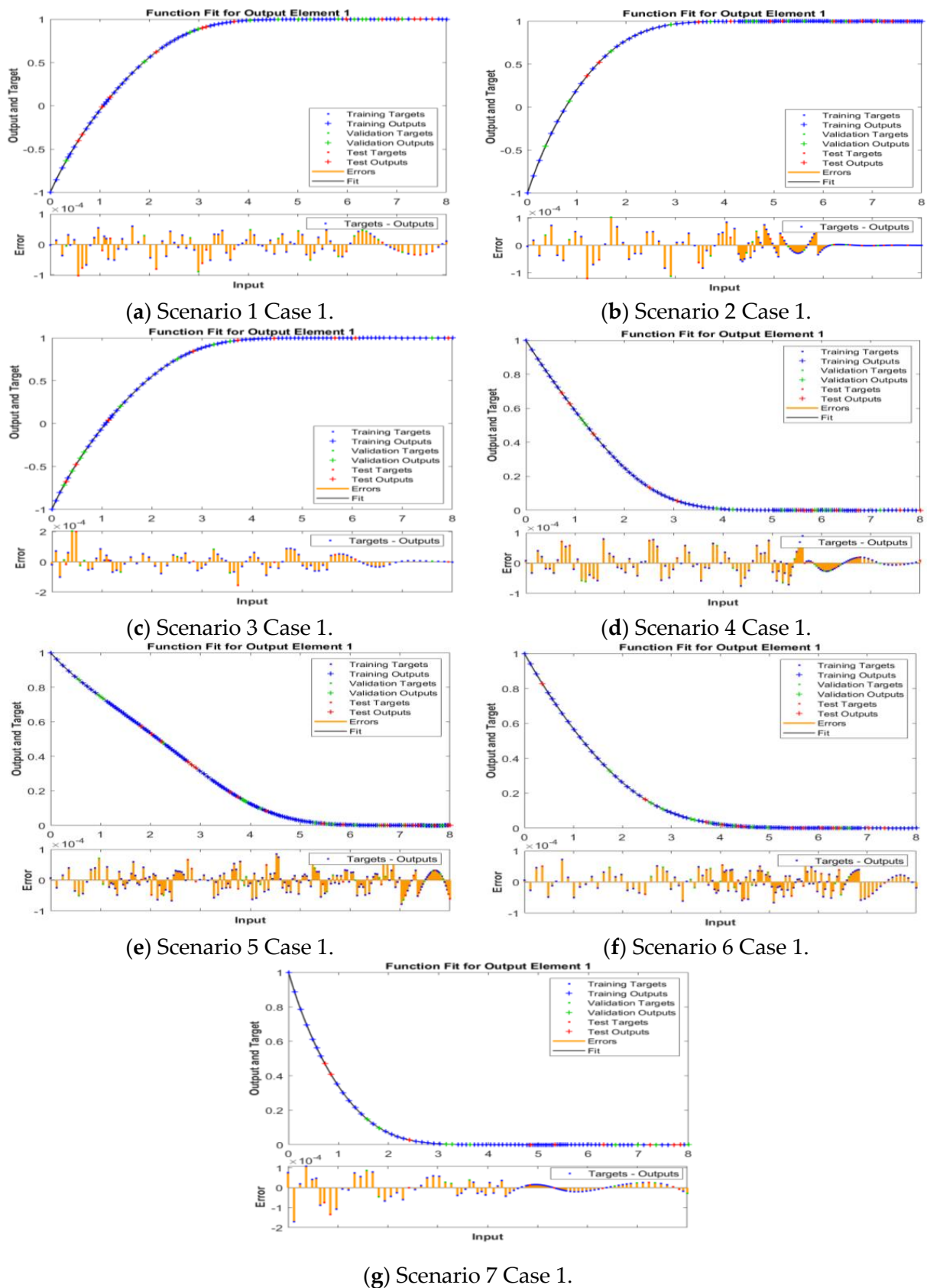


Figure 6. Fitness function of Scenarios 1–7 for Case 1 with intended LMS–BPNN.

Table 2. Data analysis of the physical pertained parameters.

Scenario	Case	MSE Level			Performance	Gradient	Mu	Epoch	T
		Training	Validation	Testing					
1	1	8.6689×10^{-10}	6.8026×10^{-10}	1.8599×10^{-9}	8.67×10^{-10}	1.36×10^{-8}	1.00×10^{-9}	462	4
	2	5.2037×10^{-10}	1.6579×10^{-9}	1.19067×10^{-9}	5.20×10^{-10}	9.98×10^{-9}	1.00×10^{-9}	654	7
	3	8.3986×10^{-10}	1.93362×10^{-9}	1.33751×10^{-9}	8.40×10^{-10}	9.96×10^{-8}	1.00×10^{-9}	693	9
2	1	1.64052×10^{-9}	3.20122×10^{-9}	1.76519×10^{-9}	1.64×10^{-9}	9.97×10^{-8}	1.00×10^{-9}	369	3
	2	7.9217×10^{-10}	1.4547×10^{-9}	2.3372×10^{-9}	7.92×10^{-10}	7.79×10^{-9}	1.00×10^{-9}	412	4
	3	9.08334×10^{-10}	9.72836×10^{-9}	3.7889×10^{-9}	9.06×10^{-10}	9.95×10^{-8}	1.00×10^{-9}	597	7
3	1	1.03437×10^{-9}	1.24016×10^{-9}	8.2608×10^{-10}	1.03×10^{-9}	9.99×10^{-9}	1.00×10^{-9}	642	8
	2	1.91010×10^{-9}	5.09625×10^{-9}	5.26224×10^{-8}	1.91×10^{-9}	9.92×10^{-9}	1.00×10^{-8}	510	6
	3	5.72994×10^{-10}	9.8458×10^{-9}	4.7515×10^{-7}	5.72×10^{-10}	9.15×10^{-7}	1.00×10^{-8}	448	5
4	1	9.34608×10^{-10}	3.08313×10^{-9}	4.1625×10^{-9}	9.35×10^{-10}	9.94×10^{-10}	1.00×10^{-10}	542	6
	2	8.6976×10^{-10}	1.3776×10^{-9}	1.51617×10^{-8}	8.70×10^{-10}	9.99×10^{-8}	1.00×10^{-9}	661	7
	3	9.9585×10^{-10}	2.0020×10^{-9}	1.7709×10^{-9}	9.96×10^{-10}	9.98×10^{-8}	1.00×10^{-9}	543	6
5	1	8.56423×10^{-10}	1.21829×10^{-9}	1.3627×10^{-9}	8.56×10^{-10}	9.71×10^{-8}	1.00×10^{-9}	215	2
	2	2.21911×10^{-9}	2.9967×10^{-8}	6.05811×10^{-9}	2.22×10^{-9}	1.00×10^{-7}	1.00×10^{-7}	268	2
	3	5.8907×10^{-10}	7.7416×10^{-10}	3.4344×10^{-9}	5.89×10^{-10}	9.82×10^{-8}	1.00×10^{-9}	248	2
6	1	1.08784×10^{-9}	1.80714×10^{-9}	6.5421×10^{-9}	1.08×10^{-9}	1.36×10^{-7}	1.00×10^{-9}	209	2
	2	7.4637×10^{-10}	2.3271×10^{-9}	2.1346×10^{-9}	7.46×10^{-10}	9.93×10^{-8}	1.00×10^{-8}	329	3
	3	8.4866×10^{-10}	2.8219×10^{-9}	2.7539×10^{-9}	8.49×10^{-10}	9.97×10^{-9}	1.00×10^{-9}	367	3
7	1	6.9690×10^{-10}	9.5715×10^{-9}	1.6041×10^{-9}	6.97×10^{-10}	9.95×10^{-9}	1.00×10^{-10}	286	3
	2	8.1501×10^{-10}	4.5647×10^{-9}	1.2280×10^{-9}	8.15×10^{-10}	9.99×10^{-8}	1.00×10^{-9}	470	5
	3	1.8905×10^{-9}	2.0167×10^{-9}	2.3857×10^{-9}	1.65×10^{-9}	6.36×10^{-8}	1.00×10^{-9}	292	4

The tabulated values of Mu and the gradient for the first solution of the seven scenarios are shown in Table 2. These values are [1.0×10^{-9} , 1.0×10^{-9} , 1.0×10^{-9} , 1.0×10^{-10} , 1.0×10^{-9} , 1.0×10^{-9} , and 1.0×10^{-10}] and [1.36×10^{-8} , 9.97×10^{-8} , 9.99×10^{-10} , 9.94×10^{-8} , 1.36×10^{-7} , and 9.95×10^{-9}]. The results indicate that LMS-BPNN consistently exhibits efficient convergence in all scenarios related to Eyring–Powell fluid flow over a diminishing wedge. The investigation of regression analysis is displayed in Figure 5a–g for Scenarios 1–7 of Eyring–Powell fluid flow over a porous shrinking wedge. Regression analysis serves as a means to explore correlations within the data. In Figure 5a–g, the correlation coefficient (R) is observed to be at unity, indicating an optimal model fit. When scrutinizing the numerical data sheet, the correlation coefficient (R) closely approximates unity, lending support to the efficacy of LMS-BPNN in formulating an Eyring–Powell fluid flow over a shrinking wedge. These coefficients assess the model’s fit quality and validate the modeling accuracy. Figure 6a–g display the function fit for the proposed model and it is noted that the function fits the model asymptotically.

Non-Uniqueness of Solution

The smart solution of flow behavior is obtained with AI-based LMS-BPNN for velocity ($f'(\eta)$), temperature ($\theta(\eta)$), and concentration ($\phi(\eta)$) profiles of Eyring–Powell fluid over a porous shrinking wedge. AI-based learning is crucial to handle the flow stability of shrinking and stretching surfaces. The MATLAB toolbox of ANNs (‘nftool’ command) is used to train the network for $f'(\eta)$, $\theta(\eta)$, and $\phi(\eta)$ to observe the effects of varying the physical parameters as in Table 1 (Scenarios 1–7). In this analysis, the author focus on thermo-physical properties of flow over a shrinking wedge. The effects of different pertained parameters are investigated, and a dual solution is obtained for various scenarios as shown in Table 1 with $W = 0.1$ and $\delta = 0.2$ remaining constant (see Ref. [39] for fixed parameters). The dual solution for flow output responses are shown in Figure 7(a–f) for different values of the pertained parameters as in Scenarios 1–7. The predicted solution with LMS-BPNN is obtained for different values of $\Psi = \frac{\pi}{6}, \frac{\pi}{3}, \frac{\pi}{2}$ with $M = 0.01$, $S = 0.8$, $\lambda = -1$, $Q = 0.01$, $Rd = 0.1$, $Sc = 0.5$, $K_c = 0.4$, $W = 0.1$, and $\delta = 0.2$ (as shown in Figure 7a. The values of these parameters are considered Ref. [39]). Figure 7b shows that

the solution changes its nature at critical values $\lambda_c = -1.06329, -1.097, -1.17694$, for various values of magnetic effects as shown in Scenario 2 ($M = 0.01, 0.05, 0.1$ with $\Psi = \frac{\pi}{6}$, $S = 0.8, \lambda = -1, Q = 0.01, Rd = 0.1, Sc = 0.5, W = 0.1$, and $\delta = 0.2$ remaining constant (the values of these parameters are considered Ref. [39])). It is also important to declare that with the increment in the value of M , then the solution bifurcates at maximum values of -1.17694 . Similarly, Figure 7c shows the impacts of porosity parameters on Cf_x . The solution bifurcates for $S = 0.8, 0.9, 1$ at critical values $\lambda_c = -0.8828, -0.97414, -1.06329$. Figure 7c shows that when we increase porosity parameters, then the critical values change from -0.8828 to -1.06329 . Figure 7d,e shows the effects of Q and Rd on heat transfer coefficient. In Figure 7f, we observe the impact of Sc on Sh_x . It is examined that the critical values remain the same for Scenario 7 Cases 1–3. From Figure 7, it is concluded that the flow response outcomes (Cf_x, Nu_x, Sh_x) have a dual nature. Figure 8a depicts the effects of the angle of inclination (Ψ) on $f'(\eta)$ and it is noted that the boundary layer thickness for the second solution is higher than the first solution. Figure 8b,c show the impact of Scenarios 2–3 on $f'(\eta)$. It is observed that when we increase the value of M , then the first solution of $f'(\eta)$ increases and the boundary layer thickness of the second solution increases. The dual solution is calculated at $M = 0.01, 0.05, 0.1$ with $\Psi = \frac{\pi}{6}, S = 0.8, \lambda = -1, Q = 0.01, Rd = 0.1, Sc = 0.5, K_c = 0.4, W = 0.1$, and $\delta = 0.2$ (the values of these parameters are considered Ref. [39]). Similarly, the porosity parameter (mentioned in Scenario 3) has a similar fashion to that in Scenario 2. With the enhancement in the porosity parameter, the velocity of the non-Newtonian fluid (Eyring–Powell fluid) increases. The impacts of Scenario 5 are displayed in Figure 8d. This figure shows the effects of Q on the temperature profile. Figure 8e shows the dual solution of the concentration profile against Sc . The dual solutions are calculated for Cf_x, Nu_x , and Sh_x with LMS-BPNN for variation in physical parameters for different scenarios as shown in Table 3. The non-unique nature of the solution is investigated by a vertical line test. This test shows that if a vertical line draws on a graph and it intersects at two points then the solution is non-unique. It is noted that the first and second solutions exist for $\lambda > \lambda_c$, at $\lambda = \lambda_c$ a unique solution exists while there is no solution for $\lambda < \lambda_c$ (λ_c represents the critical value).

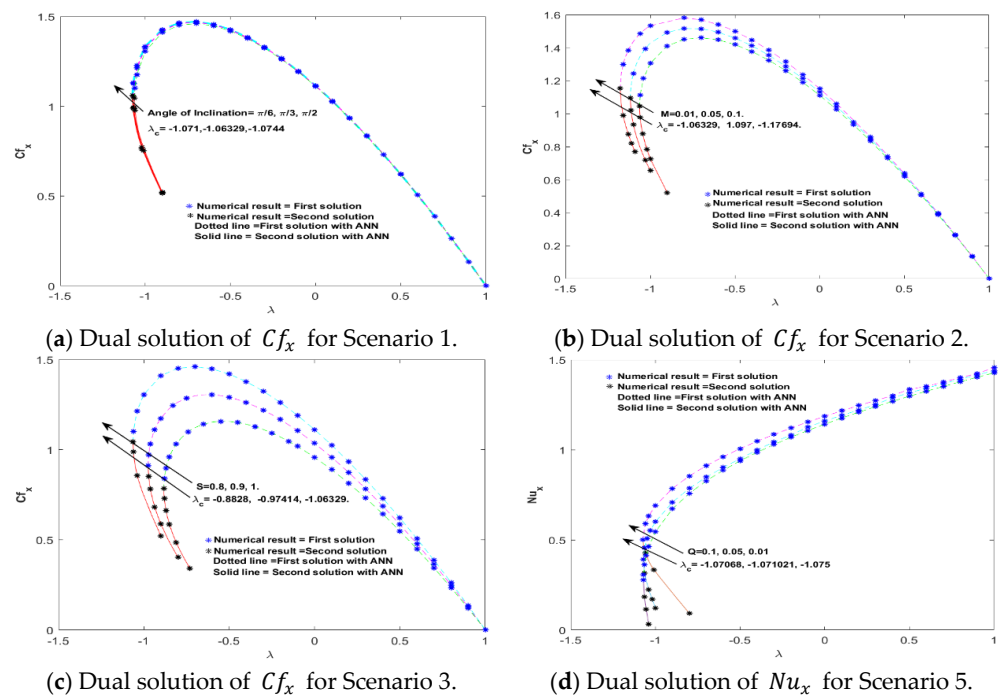
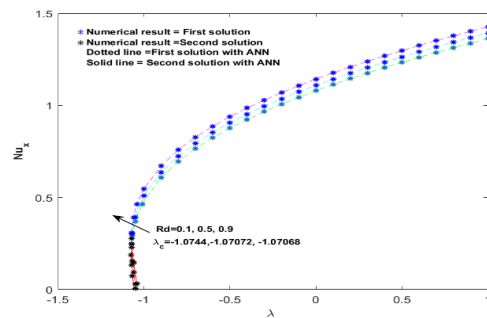
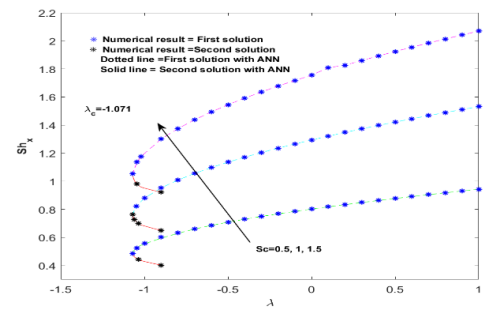


Figure 7. Cont.

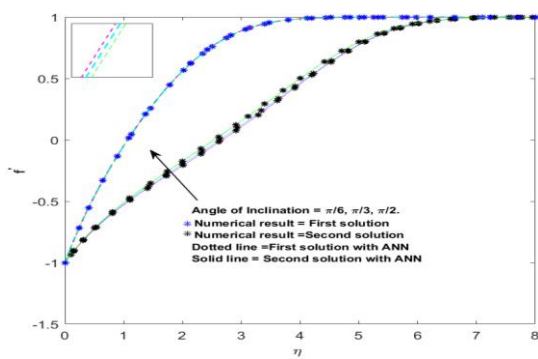


(e) Dual solution of Nu_x for Scenario 6.

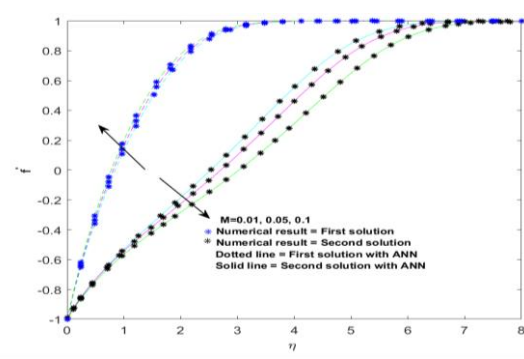


(f) Dual solution of Sh_x for Scenario 7.

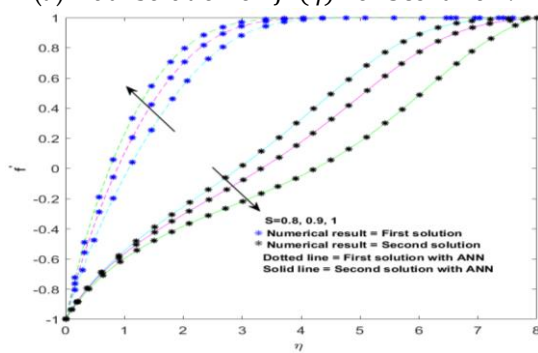
Figure 7. Non-uniqueness of the flow response quantities for various scenarios for Cases 1–3 with intended LMS–BPNN.



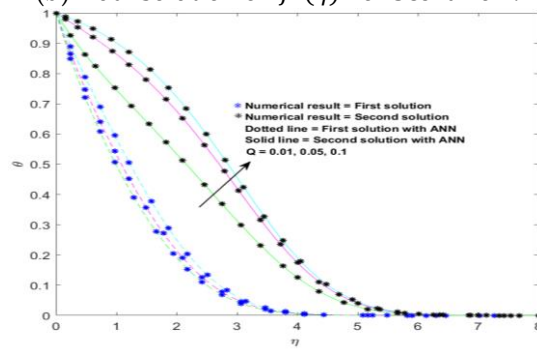
(a) Dual solution of $f'(\eta)$ for Scenario 1.



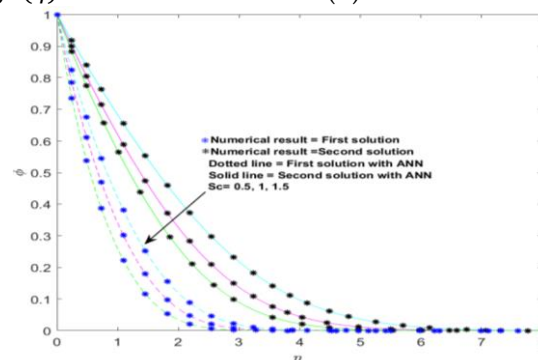
(b) Dual solution of $f'(\eta)$ for Scenario 2.



(c) Dual solution of $f'(\eta)$ for Scenario 3.



(d) Dual solution of $\theta(\eta)$ for Scenario 5.



(e) Dual solution of $\phi(\eta)$ for Scenario 7.

Figure 8. Non-uniqueness of velocity, temperature, and concentration profile for various scenarios for Cases 1–3 with intended LMS–BPNN.

Table 3. Comparison of LMS-BPNN outcomes of $f''(0)$ for different values of S .

S	(DTM-BF) [14]	Numerical [39]	Numerical [59]	Numerical [60]	LMS-BPNN
−1.5	0.96935	0.96922	0.96923	0.9692	0.96896
−1.0	0.75637	0.75657	0.75658	0.7566	0.75087
0.0	1.23350	1.23258	1.23259	1.2326	1.23186
1.0	1.88928	1.88931	1.88931	1.8893	1.87283

Figure 8d,e show the dual nature of the heat and mass transfer co-efficient for Scenarios 5 and 7. It is also concluded that porosity and magnetic effects have a high influence on flow response outcomes. When there is an increase in the values of M and S , the critical values change rapidly. Therefore, a stability test is performed to test which solution is reliable and trustworthy. Figure 9 shows the stability curve, and it is noted that the first (upper branch) solution decays and the second (lower branch) solution causes a disturbance in flow behavior. It is concluded that the upper branch solution is stable; however, the lower branch solution is unstable.

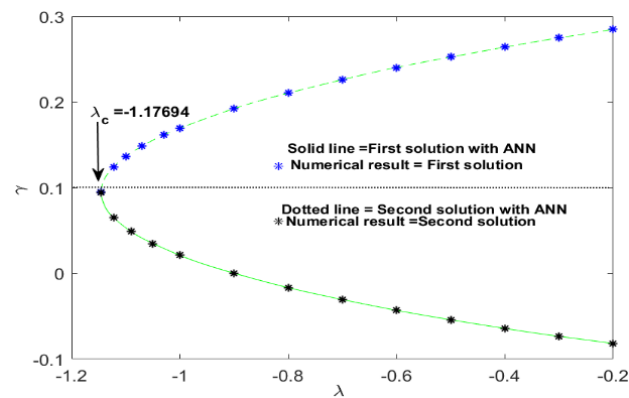


Figure 9. Stability curve.

5. Conclusions

The main goal of this research is to introduce an innovative computational intelligence method that utilizes the Levenberg–Marquardt technique with a backpropagated neural network (LMS-BPNN) to explore flow stability. A proficient conversion technique is employed on the PDEs of non-Newtonian fluid problems, transforming them into a system of ODEs. The initial/reference solution is calculated with `bvp4c` by solving the resulting system of ODEs. The labeled data set is divided into three parts: 80% is allocated for training, 10% for testing, and 10% for validation. These subsets are employed to evaluate the estimated solution derived from LMS-BPNN. The convergence of the solution is calculated utilizing the MSE, error analysis, and correlation index (R). The performance, gradient, and Mu of the LMS-BPNN are found to be 10^{-10} , 1.3610^{-8} , and 10^{-9} , respectively. The dual solution is calculated with BPNN for the different scenarios (Scenarios 1–7). The validity and consistency of the proposed LMS-BPNN are demonstrated through the presentation of table values and visual representations such as error and regression analysis. The dual solutions for $f'(\eta)$, $\theta(\eta)$, and $\phi(\eta)$ are calculated and it is observed that both solutions satisfy the boundary conditions asymptotically. The dual solution for flow performance outcomes (Cf_x , Nu_x , and Sh_x) is investigated with LMS-BPNN. It is also concluded that the critical value $\lambda_c = -1.06329$ exists at $M = 0.01$. When the magnetic effect increases, then the critical values change, i.e., $\lambda_c = -1.17694$ at $M = 0.1$. It is noticed that the boundary layer thickness for the second solution is greater than the first solution. It is also noted that the magnetic effects and porosity are flow-significant input parameters. The smart solution for stability assessment utilizes an approximation of LMS-BPNN, estimating the

eigenvalues of the flow problem. The results indicate that the first solution remains stable, while the second solution demonstrates instability. The accuracy and precision of AI-based LMS-BPNN is demonstrated by the good agreement between the predicted results with ANN and numerical results with bvp4c. In the future, unsupervised machine learning should be applied to investigate the effects of thermal properties on heat transfer analysis over a shrinking surface.

Author Contributions: Investigation, M.I.K.; methodology, A.Z.; validation, M.M.B.; writing—original draft, M.I.K.; writing—review and editing, A.Z.; formal analysis, R.E. All authors have read and agreed to the published version of the manuscript.

Funding: This research received no external funding.

Institutional Review Board Statement: Not applicable.

Informed Consent Statement: Not applicable.

Data Availability Statement: Data are contained within the article.

Conflicts of Interest: The authors declare no conflicts of interest.

Nomenclature

u_w	Velocity at wedge's wall (m.s^{-1});
u_e	Ambient velocity (m.s^{-1});
U_w, U_∞	Constant;
v_w	Suction velocity (m.s^{-1});
T	Temperature of fluid (K);
T_∞	Ambient temperature (K);
T_w	Wall temperature (K);
C_w	Concentration at wedge's wall;
C_∞	Concentration of fluid far away from a wedge;
Pr	Prandtl number;
α	Thermal diffusivity of fluid;
σ	Electrical conductivity;
Re_x	Local Reynolds number;
Cf_x	Skin friction;
Nu_x	Nusselt number;
Sh_x	Sherwood number;
Gr	Grashof number;
Gc	Mass Grashof number;
B_0	Strength of the magnetic field;
Ψ	Inclined angle (at which the magnetics field is applied);
β_0	Thermal expansion;
d	Rheological constant;
M	Magnetic field constant;
Rd	Thermal radiation;
D_B	Molecular diffusivity;
K_c	Chemical reaction parameter;
S	Suction/injection parameter;
Q	Heat generation/absorption constant;
λ	Stretching and shrinking parameter;
Sc	Schmidt number;
W, δ	Eyring–Powell fluid constant;
τ_w	Stress tensor;
γ	Eigenvalue;
PDEs	Partial differential equations;
ODEs	Ordinary differential equations;
ANN	Artificial neural network;
LMS-BPNN	Levenberg–Marquardt scheme with a backpropagation neural network;

DTM Differential transformed method;
MSE Mean squared error.

Appendix A

Validation of code;

```
function [Y,Xf,Af] = myNeuralNetworkFunction(X,~,~)
%MYNEURALNETWORKFUNCTION neural network simulation function.
%
%
% [Y] = myNeuralNetworkFunction(X,~,~) takes these arguments:
%
% X = 1xTS cell, 1 inputs over TS timesteps
% Each X{1,ts} = Qx2 matrix, input #1 at timestep ts.
%
% and returns:
% Y = 1xTS cell of 1 outputs over TS timesteps.
% Each Y{1,ts} = Qx1 matrix, output #1 at timestep ts.
%
% where Q is number of samples (or series) and TS is the number of timesteps.

%#ok<*RPMT0>

% ===== NEURAL NETWORK CONSTANTS =====

% Input 1
x1_step1.xoffset = [0;3];
x1_step1.gain = [0.333333333333333;1];
x1_step1.ymin = -1;

% Layer 1
b1 = [-2.0233281778319276434;2.7505507660415542404;4.7874361294992482385;5.81160
20445823428631];
IW1_1 = [-0.072148107843824041407;2.5537903512342152723 1.3403232535909823664];

% Layer 2
b2 = 3.1184491428184468731;
LW2_1 = [-0.28343636199198024572 -4.0103587755946596971 2.4796666138092882115];

% Output 1
y1_step1.ymin = -1;
y1_step1.gain = 2;
y1_step1.xoffset = 0;

% ===== SIMULATION =====

% Format Input Arguments
isCellX = iscell(X);
if ~isCellX
X = {X};
end

% Dimensions
TS = size(X,2); % timesteps
if ~isempty(X)
```

```

Q = size(X{1},1); % samples/series
else
Q = 0;
end

% Allocate Outputs
Y = cell(1,TS);

% Time loop
for ts=1:TS

% Input 1
X{1,ts} = X{1,ts}';
Xp1 = mapminmax_apply(X{1,ts},x1_step1);

% Layer 1
a1 = tansig_apply(repmat(b1,1,Q) + IW1_1*Xp1);

% Layer 2
a2 = repmat(b2,1,Q) + LW2_1*a1;

% Output 1
Y{1,ts} = mapminmax_reverse(a2,y1_step1);
Y{1,ts} = Y{1,ts}';

end
% Final Delay States
Xf = cell(1,0);
Af = cell(2,0);

% Format Output Arguments
if ~isCellX
Y = cell2mat(Y);
end
end

% ===== MODULE FUNCTIONS =====

% Map Minimum and Maximum Input Processing Function
function y = mapminmax_apply(x,settings)
y = bsxfun(@minus,x,settings.xoffset);
y = bsxfun(@times,y,settings.gain);
y = bsxfun(@plus,y,settings.ymin);
end

% Sigmoid Symmetric Transfer Function
function a = tansig_apply(n,~)
a = 2 ./ (1 + exp(-2*n)) - 1;
end

% Map Minimum and Maximum Output Reverse-Processing Function
function x = mapminmax_reverse(y,settings)
x = bsxfun(@minus,y,settings.ymin);
x = bsxfun(@rdivide,x,settings.gain);

```

```

x = bsxfun(@plus,x,settings.xoffset);
end
% This script assumes these variables are defined:
%
% input — input data.
% output — target data.

x = input';
t = output';
% Choose a Training Function
% For a list of all training functions type: help nntrain
% 'trainlm' is usually fastest.
% 'trainbr' takes longer but may be better for challenging problems.
% 'trainscg' uses less memory. Suitable in low memory situations.
trainFcn = 'trainlm'; % Levenberg-Marquardt backpropagation.

% Create a Fitting Network
hiddenLayerSize = 10;
net = fitnet(hiddenLayerSize,trainFcn);

```

References

- Falkner, V.M.; Skan, S.W. Some Approximate Solutions of the Boundary Layer Equations. *Philos. Mag.* **1931**, *12*, 865–896. [\[CrossRef\]](#)
- Vajravelu, K.; Nayfeh, J. Hydromagnetic convection at a cone and a wedge. *Int. Commun. Heat Mass Transf.* **1992**, *19*, 701–710. [\[CrossRef\]](#)
- Reddy, C.S.; Ali, F.; Al-Farhany, K.; Sridhar, W. Numerical analysis of gyrotactic microorganisms in MHD radiative Eyring–Powell nanofluid across a static/moving wedge with Soret and Dufour effects. *ZAMM-J. Appl. Math. Mech./Z. Für Angew. Math. Und Mech.* **2022**, *102*, e202100459. [\[CrossRef\]](#)
- Hussain, M.; Ali, A.; Ranjha, Q.A.; Ahmad, I.; Anwar, M.S. Radiative magneto-cross Eyring–Powell flow with activation energy past porous stretching wedge considering suction/injection and ohmic heating effect. *Numer. Heat Transf. Part B Fundam.* **2023**, *1–16*. [\[CrossRef\]](#)
- Gireesha, B.J.; Gorla, R.S.R.; Mahanthesh, B. Effect of suspended nanoparticles on three-dimensional MHD flow, heat and mass transfer of radiating Eyring–Powell fluid over a stretching sheet. *J. Nanofluids* **2015**, *4*, 474–484. [\[CrossRef\]](#)
- Ali, F.; Zaib, A. Unsteady flow of an Eyring–Powell nanofluid near stagnation point past a convectively heated stretching sheet. *Arab J. Basic Appl. Sci.* **2019**, *26*, 215–224. [\[CrossRef\]](#)
- Ahmed, M.F.; Zaib, A.; Ali, F.; Bafakeeh, O.T.; Tag-ElDin, E.S.M.; Guedri, K.; Khan, M.I. Numerical computation for gyrotactic microorganisms in MHD radiative Eyring–Powell nanomaterial flow by a static/moving wedge with Darcy–Forchheimer relation. *Micromachines* **2022**, *13*, 1768. [\[CrossRef\]](#) [\[PubMed\]](#)
- Sivaraj, R.; Kumar, B.R. Unsteady MHD dusty viscoelastic fluid Couette flow in an irregular channel with varying mass diffusion. *Int. J. Heat Mass Transf.* **2012**, *55*, 3076–3089. [\[CrossRef\]](#)
- Kumar, B.R.; Sivaraj, R. Heat and mass transfer in MHD viscoelastic fluid flow over a vertical cone and flat plate with variable viscosity. *Int. J. Heat Mass Transf.* **2013**, *56*, 370–379. [\[CrossRef\]](#)
- Khan, W.A.; Sultan, F.; Ali, M.; Shahzad, M.; Khan, M.; Irfan, M. Consequences of activation energy and binary chemical reaction for 3D flow of Cross-nanofluid with radiative heat transfer. *J. Braz. Soc. Mech. Sci. Eng.* **2019**, *41*, 4. [\[CrossRef\]](#)
- Lund, L.A.; Omar, Z.; Khan, I. Analysis of dual solution for MHD flow of Williamson fluid with slippage. *Heliyon* **2019**, *5*, e01345. [\[CrossRef\]](#) [\[PubMed\]](#)
- Yih, K.A. MHD forced convection flow adjacent to a non-isothermal wedge. *Int. Commun. Heat Mass Transf.* **1999**, *26*, 819–827. [\[CrossRef\]](#)
- Chamkha, A.J.; Mujtaba, M.; Quadri, A.; Issa, C. Thermal radiation effects on MHD forced convection flow adjacent to a non-isothermal wedge in the presence of a heat source or sink. *Heat Mass Transf.* **2003**, *39*, 305–312. [\[CrossRef\]](#)
- Su, X.; Zheng, L.; Zhang, X.; Zhang, J. MHD mixed convective heat transfer over a permeable stretching wedge with thermal radiation and ohmic heating. *Chem. Eng. Sci.* **2012**, *78*, 1–8. [\[CrossRef\]](#)
- Prasad, K.V.; Datti, P.S.; Vajravelu, K. MHD mixed convection flow over a permeable non-isothermal wedge. *J. King Saud Univ. Sci.* **2013**, *25*, 313–324. [\[CrossRef\]](#)
- El-Dabe, N.T.; Ghaly, A.Y.; Rizkallah, R.R.; Ewis, K.M.; Al-Bareda, A.S. Numerical solution of MHD boundary layer flow of non-Newtonian Casson fluid on a moving wedge with heat and mass transfer and induced magnetic field. *J. Appl. Math. Phys.* **2015**, *3*, 649. [\[CrossRef\]](#)

17. Hsiao, K.L. To promote radiation electrical MHD activation energy thermal extrusion manufacturing system efficiency by using Carreau-Nanofluid with parameters control method. *Energy* **2017**, *130*, 486–499. [[CrossRef](#)]
18. Awaludin, I.S.; Ishak, A.; Pop, I. On the stability of MHD boundary layer flow over a stretching/shrinking wedge. *Sci. Rep.* **2018**, *8*, 13622. [[CrossRef](#)] [[PubMed](#)]
19. Anuar, N.S.; Bachok, N.; Arifin, N.M.; Rosali, H. Effect of suction/injection on stagnation point flow of hybrid nanofluid over an exponentially shrinking sheet with stability analysis. *CFD Lett.* **2019**, *11*, 21–33.
20. Waini, I.; Ishak, A.; Pop, I. MHD flow and heat transfer of a hybrid nanofluid past a permeable stretching/shrinking wedge. *Appl. Math. Mech.* **2020**, *41*, 507–520. [[CrossRef](#)]
21. Mustafa, I.; Abbas, Z.; Arif, A.; Javed, T.; Ghaffari, A. Stability analysis for multiple solutions of boundary layer flow towards a shrinking sheet: Analytical solution by using least square method. *Phys. A Stat. Mech. Its Appl.* **2020**, *540*, 123028. [[CrossRef](#)]
22. Kasmani, R.M.; Sivasankaran, S.; Bhuvanewari, M.; Siri, Z. Effect of chemical reaction on convective heat transfer of boundary layer flow in nanofluid over a wedge with heat generation/absorption and suction. *J. Appl. Fluid Mech.* **2015**, *9*, 379–388. [[CrossRef](#)]
23. Kamal, F.; Zaimi, K.; Ishak, A.; Pop, I. Stability analysis of MHD stagnation-point flow towards a permeable stretching/shrinking sheet in a nanofluid with chemical reactions effect. *Sains Malays.* **2019**, *48*, 243–250. [[CrossRef](#)]
24. Zainal, N.A.; Nazar, R.; Naganthran, K.; Pop, I. Stability analysis of MHD hybrid nanofluid flow over a stretching/shrinking sheet with quadratic velocity. *Alex. Eng. J.* **2021**, *60*, 915–926. [[CrossRef](#)]
25. Mishra, M.R.; Hussain, S.M.; Makinde, O.D.; Seth, G.S. Stability analysis and multiple solutions of a hydromagnetic dissipative flow over a stretching/shrinking sheet. *Bulg. Chem. Commun.* **2020**, *52*, 259–271.
26. Hamid, M.; Usman, M.; Khan, Z.H.; Ahmad, R.; Wang, W. Dual solutions and stability analysis of flow and heat transfer of Casson fluid over a stretching sheet. *Phys. Lett. A* **2019**, *383*, 2400–2408. [[CrossRef](#)]
27. Arani, A.A.A.; Aberoumand, H. Stagnation-point flow of Ag-CuO/water hybrid nanofluids over a permeable stretching/shrinking sheet with temporal stability analysis. *Powder Technol.* **2021**, *380*, 152–163. [[CrossRef](#)]
28. Lund, L.A.; Omar, Z.; Khan, I.; Sherif, E.S.M. Dual solutions and stability analysis of a hybrid nanofluid over a stretching/shrinking sheet executing MHD flow. *Symmetry* **2020**, *12*, 276. [[CrossRef](#)]
29. Zeeshan, A.; Khan, M.I.; Ellahi, R.; Marin, M. Computational Intelligence Approach for Optimising MHD Casson Ternary Hybrid Nanofluid over the Shrinking Sheet with the Effects of Radiation. *Appl. Sci.* **2023**, *13*, 9510. [[CrossRef](#)]
30. Reddy, P.B.A.; Das, R. Estimation of MHD boundary layer slip flow over a permeable stretching cylinder in the presence of chemical reaction through numerical and artificial neural network modeling. *Eng. Sci. Technol. Int. J.* **2016**, *19*, 1108–1116. [[CrossRef](#)]
31. Shoaib, M.; Kausar, M.; Nisar, K.S.; Raja, M.A.Z.; Morsy, A. Impact of thermal energy on MHD Casson fluid through a Forchheimer porous medium with inclined non-linear surface: A soft computing approach. *Alex. Eng. J.* **2022**, *61*, 12211–12228. [[CrossRef](#)]
32. Awais, M.; Raja, M.A.Z.; Awan, S.E.; Shoaib, M.; Ali, H.M. Heat and mass transfer phenomenon for the dynamics of Casson fluid through porous medium over shrinking wall subject to Lorentz force and heat source/sink. *Alex. Eng. J.* **2021**, *60*, 1355–1363. [[CrossRef](#)]
33. Reddy, S.R.R.; Sekhar, K.R.; Charupalli, S.K.; Jakeer, S.; Lakshmi Rupa, M.; Manikandan, K.; Mahesh Kumar, T. Impact of Arrhenius activation energy on magnetic nanofluid flow over a slendering stretchable sheet with nonlinear radiative heat transfer: A machine learning algorithm. *Numer. Heat Transf. Part B Fundam.* **2024**, 1–23. [[CrossRef](#)]
34. Mishra, A.; Rawat, S.K.; Yaseen, M.; Pant, M. Development of machine learning algorithm for assessment of heat transfer of ternary hybrid nanofluid flow towards three different geometries: Case of artificial neural network. *Heliyon* **2023**, *9*, e21453. [[CrossRef](#)] [[PubMed](#)]
35. Zeeshan, A.; Khan, M.I.; Ellahi, R.; Asghar, Z. Artificial neural network simulation and sensitivity analysis for optimal thermal transport of magnetic viscous fluid over shrinking wedge via RSM. *Int. J. Numer. Methods Heat Fluid Flow* **2023**, *33*, 3492–3518. [[CrossRef](#)]
36. Ishtiaq, F.; Ellahi, R.; Bhatti, M.M.; Alamri, S.Z. Insight in thermally radiative cilia-driven flow of electrically conducting non-Newtonian Jeffrey fluid under the influence of induced magnetic field. *Mathematics* **2022**, *10*, 2007. [[CrossRef](#)]
37. Ellahi, R.; Alamri, S.Z.; Basit, A.; Majeed, A. Effects of MHD and slip on heat transfer boundary layer flow over a moving plate based on specific entropy generation. *J. Taibah Univ. Sci.* **2018**, *12*, 476–482. [[CrossRef](#)]
38. Ellahi, R. The effects of MHD and temperature dependent viscosity on the flow of non-Newtonian nanofluid in a pipe: Analytical solutions. *Appl. Math. Model.* **2013**, *37*, 1451–1457. [[CrossRef](#)]
39. Hussain, M.; Ranjha, Q.A.; Anwar, M.S.; Jahan, S.; Ali, A. Eyring-Powell model flow near a convectively heated porous wedge with chemical reaction effects. *J. Taiwan Inst. Chem. Eng.* **2022**, *139*, 104510. [[CrossRef](#)]
40. Raju, C.S.K.; Sandeep, N. Nonlinear radiative magnetohydrodynamic Falkner-Skan flow of Casson fluid over a wedge. *Alex. Eng. J.* **2016**, *55*, 2045–2054. [[CrossRef](#)]
41. Kumar, K.A.; Ramadevi, B.; Sugunamma, V.; Reddy, J.R. Heat transfer characteristics on MHD Powell-Eyring fluid flow across a shrinking wedge with non-uniform heat source/sink. *J. Mech. Eng. Sci.* **2019**, *13*, 4558–4574. [[CrossRef](#)]
42. Kumari, M.; Jain, S. MHD Convective Boundary Layer Falkner-Skan Flow for Powell-Eyring Fluid Over a Permeable Moving Wedge with Heat Source. *J. Nanofluids* **2019**, *8*, 938–946. [[CrossRef](#)]

43. Agrawal, P.; Dadheech, P.K.; Jat, R.N.; Nisar, K.S.; Bohra, M.; Purohit, S.D. Magneto Marangoni flow of γ - Al_2O_3 nanofluids with thermal radiation and heat source/sink effects over a stretching surface embedded in porous medium. *Case Stud. Therm. Eng.* **2021**, *23*, 100802. [[CrossRef](#)]
44. Azam, M. Effects of Cattaneo-Christov heat flux and nonlinear thermal radiation on MHD Maxwell nanofluid with Arrhenius activation energy. *Case Stud. Therm. Eng.* **2022**, *34*, 102048. [[CrossRef](#)]
45. Abdal, S.; Siddique, I.; Alshomrani, A.S.; Jarad, F.; Din, I.S.U.; Afzal, S. Significance of chemical reaction with activation energy for Riga wedge flow of tangent hyperbolic nanofluid in existence of heat source. *Case Stud. Therm. Eng.* **2021**, *28*, 101542. [[CrossRef](#)]
46. Bush, A. *Perturbation Methods for Engineers and Scientists*; Routledge: London, UK, 2018.
47. Weidman, P.D.; Kubitschek, D.G.; Davis, A.M.J. The effect of transpiration on self-similar boundary layer flow over moving surfaces. *Int. J. Eng. Sci.* **2006**, *44*, 730–737. [[CrossRef](#)]
48. Zaimi, K.; Ishak, A.; Pop, I. Unsteady flow of a nanofluid past a permeable shrinking cylinder using Buongiorno's model. *Sains Malays.* **2017**, *46*, 1667–1674. [[CrossRef](#)]
49. Othman, N.A.; Yacob, N.A.; Bachok, N.; Ishak, A.; Pop, I. Mixed convection boundary-layer stagnation point flow past a vertical stretching/shrinking surface in a nanofluid. *Appl. Therm. Eng.* **2017**, *115*, 1412–1417. [[CrossRef](#)]
50. Awaludin, I.S.; Ahmad, R.; Ishak, A. On the stability of the flow over a shrinking cylinder with prescribed surface heat flux. *Propuls. Power Res.* **2020**, *9*, 181–187. [[CrossRef](#)]
51. Ghosh, S.; Mukhopadhyay, S. Stability analysis for model-based study of nanofluid flow over an exponentially shrinking permeable sheet in presence of slip. *Neural Comput. Appl.* **2020**, *32*, 7201–7211. [[CrossRef](#)]
52. Merrill, K.; Beauchesne, M.; Previte, J.; Poullet, J.; Weidman, P. Final steady flow near a stagnation point on a vertical surface in a porous medium. *Int. J. Heat Mass Transf.* **2006**, *49*, 4681–4686. [[CrossRef](#)]
53. Hecht-Nielsen, R. Neurocomputer applications. In *Neural Computers*; Springer: Berlin/Heidelberg, Germany, 1989; pp. 445–453.
54. Jakeer, S.; Rupa, M.L.; Reddy, S.R.R.; Rashad, A.M. Artificial neural network model of non-Darcy MHD Sutterby hybrid nanofluid flow over a curved permeable surface: Solar energy applications. *Propuls. Power Res.* **2023**, *12*, 410–427. [[CrossRef](#)]
55. McCulloch, W.S.; Pitts, W. A logical calculus of the ideas immanent in nervous activity. *Bull. Math. Biophys.* **1943**, *5*, 115–133. [[CrossRef](#)]
56. Chakraverty, S.; Mall, S. *Artificial Neural Networks for Engineers and Scientists: Solving Ordinary Differential Equations*; CRC Press: Boca Raton, FL, USA, 2017.
57. Reddy, S.R.R.; Jakeer, S.; Rupa, M.L. ANN model of three-dimensional micropolar dusty hybrid nanofluid flow with coriolis force: Biomedical applications. *Indian J. Phys.* **2023**, *97*, 3801–3825. [[CrossRef](#)]
58. Anand, A.V.; Ali, R.; Jakeer, S.; Reddy, S.R.R. Entropy-optimized MHD three-dimensional solar slendering sheet of micropolar hybrid nanofluid flow using a machine learning approach. *J. Therm. Anal. Calorim.* **2023**, 1–23. [[CrossRef](#)]
59. Yih, K.A. Uniform suction/blowing effect on forced convection about a wedge: Uniform heat flux. *Acta Mech.* **1998**, *128*, 173–181. [[CrossRef](#)]
60. Ishak, A.; Nazar, R.; Pop, I. Falkner-Skan equation for flow past a moving wedge with suction or injection. *J. Appl. Math. Comput.* **2007**, *25*, 67–83. [[CrossRef](#)]

Disclaimer/Publisher's Note: The statements, opinions and data contained in all publications are solely those of the individual author(s) and contributor(s) and not of MDPI and/or the editor(s). MDPI and/or the editor(s) disclaim responsibility for any injury to people or property resulting from any ideas, methods, instructions or products referred to in the content.